# MULTI-PICOSECOND HO:YLF-PUMPED SUPERCONTINUUM GENERATION AND $ZNGEP_2$-BASED OPTICAL PARAMETRIC AMPLIFIERS IN THE FINGERPRINT REGIME


Dissertation
Zur Erlangung des Doktorgrades
an der Fakultät für Mathematik, Informatik und Naturwissenschaften
Fachbereich Physik
der Universität Hamburg

vorgelegt von
SIQI CHENG

Hamburg
15.12.2020

Siqi Cheng:
*Multi-picosecond Ho:YLF-pumped supercontinuum generation and $ZnGeP_2$-based optical parametric amplifiers in the fingerprint regime*

Gutachter der Dissertation:
Prof. Dr. R. J. Dwayne Miller
Prof. Dr. Franz X. Kärtner

Zusammensetzung der Prüfungskommission:
Prof. Dr. R. J. Dwayne Miller
Prof. Dr. Franz X. Kärtner
Prof. Dr. Nils Huse
Prof. Dr. Henry Chapman
Prof. Dr. Daniela Pfannkuche

Vorsitzende der Prüfungskommission:
Prof. Dr. Daniela Pfannkuche

Vorsitzender Fach-Promotionsausschusses PHYSIK:
Prof. Dr. Günter Hans Walter Sigl

Leiter des Fachbereichs PHYSIK:
Prof. Dr. Wolfgang Hansen

Dekan der Fakultät MIN:
Prof. Dr. Heinrich Graener

Location: Hamburg

Datum der Disputation: 15.12.2020

To my beloved family.

# ABSTRACT

In this thesis, an ultrafast optical parametric amplification (OPA) system with a pair of OPA chains which can be independently tuned in mid-infrared (MIR) range ( 3-8 $\mu$m) is demonstrated. Various coherent ultrafast MIR laser sources have been widely applied in the field of physics and chemistry. This interest is largely driven by the fact that the coherent tunable ultrashort MIR laser pulses can be utilized in vibrationally controlled chemistry and study of chemical dynamics due to their direct accessibility of the vibrational modes of various molecules and in the capability of resolving ultrafast chemical dynamics.

The OPA system consists of a home-built Ho:YLF regenerative amplifier (RA) at 2 $\mu$m for pumping, a supercontinuum (SC) stage for the parametric seeding, and a pair of cascaded OPA stages for difference-frequency generation (DFG)/OPA in the MIR region.

Due to the relatively long, 3 ps, pulse duration of the output of the RA, the seed for parametric amplification from the SC generation in the bulk medium is subject to detrimental avalanche ionization (AI) in pumping with long-duration (> picosecond) pulses. With the help of an extreme-loose focusing geometry (numerical aperture as low as $\sim$ 0.005 ), the plasma-induced damage is avoided. Multi-octave SC is successfully generated in a 15cm-long ytrrium aluminum garnet (YAG) crystal. Comparisons between different bulk media, i.e., YAG, zinc selenide (ZnSe) and gallium arsenide (GaAs) under identical conditions are conducted. YAG-based SC and ZnSe-based SC are used as the seed for an OPA stage. In this application, ZnSe-based SC is preferred due to its better performance of the suppression on the modulation instability and the pulse splitting effect.

The non-oxide zinc germanium phosphide (ZGP) crystals are employed in the ultrafast OPA system due to their impressive high nonlinearity (77-81 pm/V). Preliminary simulation on the optimization of the amplification gain in single OPA stage is carried out with Chi2D software. Critical thresholds of parameters such as optical intensity, spatial and temporal overlap of pulses,

for initiating back conversion is mapped out as well. Experimentally, in order to cover chemically relevant spectral ranges, a pair of cascaded ZGP-based OPA lines shared with the same SC from ZnSe crystal are developed. Each OPA line can be independently tuned to generate MIR pulses between 3 to 8 $\mu$m (signal & idler). Dispersion management for the idler is optimized with bulk germanium (Ge) for pulse compression. Pulse duration of the idler is compressed from $\sim$ 0.5 ps down to 105 fs at 5 $\mu$m, which proves the feasibility of the pulse compression with bulk medium. The influence of back conversion or cascaded $\chi^{(2)}$ effects is simulated with Chi2D, which corroborates with the experimental results. The correlation between the simulations and the experiments maybe useful for further optimization in increasing the idler energy without imposing difficulties in pulse compression.

Further improvements in scaling of the pulse energy and stability of the pulses are expected in the near further by using large-aperture ZGP crystals for successive OPA/OPCPA stages. This development holds promise to provide a pivotal influence in exploring nonlinear vibrational couplings to reaction coordinates in ultrafast molecular dynamics that have so far been largely limited by the available energy of the MIR driver at the required wavelengths.

# ZUSAMMENFASSUNG

In dieser Arbeit wird ein ultraschnelles optisches parametrisches Verstärkungssystem (OPA) bestehend aus zwei verketteten OPAs, die unabhängig voneinander im mittleren Infrarot (MIR) abgestimmt werden können ( 3-8 $\mu$m), vorgestellt.

Einsatzbereiche für ultraschnelle MIR-Laserquellen erstrecken sich auf weite Bereiche in Physik und Chemie. Insbesondere die kohärenten, durchstimmbaren und ultrakurzen MIR-Laserpulse können aufgrund ihrer Eigenschaften die Zugänglichkeit zu Schwingungsmoden verschiedener Moleküle vereinfachen und zur Auflösung ultraschneller chemischer Dynamik in der vibrational kontrollierten Chemie und chemischen Spektroskopie eingesetzt werden. Das OPA-System besteht aus einem neu entwickelten regenerativen, bei 2 $\mu$m gepumpten, Ho:YLF-Verstärker (RA), einer Stufe zur Erzeugung eines Superkontinuums (SC) für das parametrische Seeding und einem Paar kaskadierter OPA-Stufen zur Differenzfrequenzerzeugung (DFG)/OPA im MIR-Bereich.

Da die Pulsdauer der Ausgangspulse des RA ca. 3 ps beträgt, neigt der Seed-Strahl für die parametrische Verstärkung aus dem SC im Bulkmedium beim Pumpen mit langanhaltenden (> Pikosekunde) Pulsen zu einer schädlichen Lawinen-Ionisation (AI). Mit Hilfe einer absichtlich unscharfen Fokussierungsgeometrie (numerische Apertur bis hinunter zu 0.005 ) wird eine plasmainduzierte Schädigung vermieden. Mehrere Oktaven umspannendes SC wird erfolgreich in einem 15 cm langen YAG-Kristall erzeugt. In der Arbeit werden Vergleiche zwischen verschiedenen Bulkmedien wie YAG, ZnSe oder GaAs unter identischen Bedingungen durchgeführt. SC auf YAG-Basis und ZnSe-Basis werden als Seed-Strahl für die OPA-Stufe verwendet. SC auf ZnSe-Basis wird wegen seiner besseren Eignung in der Unterdrückung der Modulationsinstabilität und des Impulsaufspaltungseffekts für diese Arbeit bevorzugt.

Oxidfreie Zink-Germanium-Phosphid (ZGP)-Kristalle werden auf Grund ihrer beeindruckend hohen Nichtlinearität (77-81 pm/V) im ultraschnellen OPA-System eingesetzt. Vorläufige Si-

mulationen zur Optimierung der Verstärkung in den einzelnen OPA-Stufen wurden mit Chi2D-Software durchgeführt. Kritische Schwellenwerte von Parametern wie optischer Intensität oder der räumlichen und zeitlichen Überlappung der Pulse zur Einleitung der Rückkonversion werden ebenfalls abgebildet. Für Anwendungen in der Chemie und damit verbundenen Wellenlängenbereiche wurden experimentell zwei kaskadierte ZGP-basierte OPA-Linien entwickelt, die sich das SC aus ZnSe -Kristall teilen. Jede OPA-Linie kann unabhängig voneinander auf die Erzeugung von MIR Impulsen zwischen 3 bis 8 $\mu$m abgestimmt werden (Signal & Idler). Das Dispersionsmanagement für den Idler-Strahl wird mittels Germanium-Komponenten auf Pulskompression hin optimiert. Die Pulsdauer des Idler-Strahles wird von um 0,5 ps auf 105 fs bei 5 $\mu$m komprimiert, was die Machbarkeit der Pulskompression mit Hilfe eines Bulkmediums beweist. Der Einfluss von Rückkonversionen oder kaskadierten $\chi^{(2)}$-Effekten wurde mit Chi2D simuliert und es wurde Übereinstimmung zu den experimentellen Ergebnissen gefunden. Die gute Korrelation zwischen den Simulationen und den experimentellen Daten könnte sich für eine weitere Erhöhung der Energie des Idler-Strahles nützlich erweisen unter Umgehung von Schwierigkeiten bei der Pulskompression.

Weitere Verbesserungen zur Skalierung der Impulsenergie und der Stabilität der Pulse werden in naher Zukunft durch die Verwendung von ZGP-Kristallen mit großer Apertur für aufeinander folgende OPA/OPCPA-Stufen erwartet. Dies könnte einen entscheidenden Einfluss auf die Erforschung nichtlinearer Schwingungskopplungen in der ultraschnellen Molekulardynamik haben, die bisher durch die verfügbare Energie des Mittelinfrarot-Treibers bei den erforderlichen Wellenlängen eingeschränkt waren.

# PUBLICATIONS

1. **Siqi Cheng**, Gourab Chatterjee, Friedjof Tellkamp, Axel Ruehl, and R. J. Dwayne Miller, *Multi-octave supercontinuum generation in YAG pumped by mid-infrared, multi-picosecond pulses*, Optics Letters 43, no. 18 (2018): 4329.

2. **Siqi Cheng**, Gourab Chatterjee, Friedjof Tellkamp, Tino Lang, Axel Ruehl, Ingmar Hartl, and R. J. Dwayne Miller, *Compact Ho:YLF-pumped $ZnGeP_2$-based optical parametric amplifiers tunable in the molecular fingerprint regime*, Optics Letters 45, no. 8 (2020): 2255.

3. **Siqi Cheng**, Gourab Chatterjee, Friedjof Tellkamp, Axel Ruehl, and R. J. Dwayne Miller, *Overcoming avalanche ionization to generate multi-octave supercontinuum pumped by a Ho: YLF regenerative amplifier*, The European Conference on Lasers and Electro-Optics. Optical Society of America, 2019.

# ACKNOWLEDGMENTS

I would like to thank Prof. R. J. Dwayne Miller for offering me the valuable opportunity to be a Ph.D. student in his group. I thank him for his instructive discussion in every meeting and his tolerance to failures.

I would also like to thank Dr. Gourab Chatterjee, especially for his supervision on a daily basis. He has always been a reliable team mate for sharing with me his useful experience in experiments, scientific writing and for his critical suggestions in every critical stage of the project. Without his supervision, I would not have accomplished these achievements, which are beyond my expectations.

Many thanks to Dr. Axel Ruehl for his critical opinions on the revision of the two important journal papers that I published.

Special thanks go to Prof. Franz X. Kaertner for his support in the co-operation between me and his group, which provided me more opportunities to learn more beyond my project.

I want to thank Dr. Huseyin Cankaya and Dr. Yizhou Liu from Prof. Kaertner's group for their generous help in laser building and laser maintenance.

Many thanks to the support from Dr. Tino Lang from Prof. Ingmar Hartl for his generosity in sharing his knowledgeable experience on simulations. I appreciate the help from Sarper Salman and Christoph Mahnke in the maintenance of the fiber oscillator as well.

Further appreciation goes to the technical support from Friedjof Tellkamp, Hendrik Schikora, Jan-Philipp Leimkohl and Djordje Gitaric. It is always pleasant to work with you. Without your support, my Ph.D. life would take much longer.

I also thank the support from IMPRS-UFAST. I sincerely appreciate the patient and kind help from Julia Quante, Neda Lotfiomran and Charlotte Wintgens, especially during the very beginning and the final course of my Ph.D. life. Without your assistance, things would be more difficult for me.

I sincerely appreciate the endeavor from Dagmar Schröder-Huse for her steady support in maintaining an internationally friendly environment in MPSD. I also appreciate the help from the H.R. department and the purchasing department for their useful assistance and clear explanation to every question I had.

Finally, I want to say 'I love you' to my families back in China. Without your support, I would not have been able to make it.

# CONTENTS

# LIST OF FIGURES

## LIST OF TABLES

# ACRONYMS

AGS silver gallium sulphide

AI avalanche ionization

AOM acousto-optic modulator

BBO barium borate

CEP carrier-envelope phase

CP critical power

CPA chirped pulse amplification

CSP cadmium silicon phosphide

CVBG chirped volume Bragg grating

DFG difference-frequency generation

DM dichroic mirror

FROG frequency-resolved optical gating

FTL fourier transform limit

FWHM full width at half maximum

GaAs gallium arsenide

GaSe gallium selenide

Ge germanium

HHG high-harmonic generation

KTA potassium titanyle arsenate

LGS langasite

LIED laser-induced electron diffraction

LWFA laser wakefield acceleration

LWIR long-wave infrared

MCT cadmium mercury telluride

MI modulation instability

MIR mid-infrared

MPI multiphoton ionization

MWIR mid-wave infrared

NA numerical aperture

OPA optical parametric amplification

OPCPA optical parametric chirped pulse amplification

OR optical rectification

PMA phase-matching angle

PPLN periodically poled lithium niobate

QCL quantum cascade laser

RA regenerative amplifier

SC supercontinuum

SF self focusing

SFG sum frequency generation

SHG second harmonic generation

SLM spatial light modulator

SPM self phase modulation

SWIR short-wave infrared

THG third-harmonic generation

TI tunneling ionization

TOD third-order dispersion

YAG ytrrium aluminum garnet

ZnSe zinc selenide

ZGP zinc germanium phosphide

V

# Part I

# 1

# INTRODUCTION

Mid-infrared (MIR) is generally referred to the spectral range between 2.5 and 25 $\mu$m. Coherent ultrafast laser sources in this range are of great interest to scientists in various fields, such as strong-field physics and ultrafast spectroscopy in chemistry.

## 1.1 APPLICATIONS

Intense ultrashort MIR laser pulses have been keenly pursued and applied in strong-field physics and attosecond ($10^{-18}$ s) science in recent decades, especially in the creation of attosecond pulses through high-harmonic generation (HHG). Attosecond laser pulses can be used to trace ultrafast electronic and structural dynamics of matter. In the HHG process, the ponderomotive energy of the liberated electron ($U_p$) is proportional to the square of the driving wavelength ($\lambda^2$) and the pump intensity ($I$). The corresponding cut-off photon energy of the high harmonics is governed by $h\nu_{max} = I_p + U_p$, where $U_p \propto I\,\lambda^2$. For example, assisted with intense few-cycle MIR optical parametric chirped pulse amplification (OPCPA) at 4 $\mu m$ and a high-pressure gas-filled waveguide, the Kapteyn-Murnane group has obtained an impressive phase-matched HHG with one of the highest photon energies recorded to date – up to 1.6 kilo-electron volts (keV) [1]. Moreover, high-intensity ultrashort MIR lasers are also favored in the manipulation of electrons, such as laser-induced electron diffraction (LIED) and laser wakefield acceleration (LWFA) of electrons. In the LIED experiments, intense ultrashort pulses in the MIR region can quadratically scale the re-scattering energy of the electrons at longer wavelengths, leading to larger momentum transfers so that the structural information of the molecules can be extracted with a higher spatial resolution [2]. Concerning LWFA, the critical plasma density required for 'wakefield' acceleration is inversely quadratically proportional to the driving wavelength.

Hence, the lower critical threshold at longer wavelengths makes it easier for scientists to conduct experiments and simplify the experimental design for LWFA [3].

One of the major applications of ultrashort MIR laser pulses is in ultrafast vibrational spectroscopy [4]. Because the frequencies of molecular vibrations are dependent on the molecular structure and the surrounding environment, the MIR absorption spectra carry unique information about molecular structure [5]. Thus, the range of molecular absorption frequencies in the 2-20 $\mu m$ region is also called the 'fingerprint' region. Therefore, by using high-energy high-repetition-rate ultrashort MIR lasers in pump-probe spectroscopic techniques, chemists can probe specific vibrational modes and extract time-resolved information on the structural dynamics of the chemical or biological processes [4, 5].

Intense ultrashort MIR laser pulses are also of importance for laser-selective chemistry. Chemists can use these laser pulses to selectively excite key vibrational modes, which are closely linked to the reaction pathway. For instance, researchers can use the ultrashort IR pulses to control the vibrational modes coupled to the electron transfer in donor-bridge-acceptor molecules and thereby alter the yield of products in the chemical reaction that follows[6]. Moreover, chemists can also shape the phase and the amplitude of the intense MIR laser pulses depending on the potential energy surface of the molecule, so that they can selectively excite one or multiple vibrational modes [7, 8]. Nowadays, various novel high-intensity ultrashort MIR laser sources have been developed and applied in various research areas. Most current commercial ultrashort MIR laser systems are constrained with respect to wavelength tunability or in terms of available energy (< few $\mu$J) of the MIR output. Hence, the flexibility of the design and the efficiency of the experiments is largely restrained by the limited performance of available laser systems in the MIR range.

This thesis aims at the development of a coherent high-intensity femtosecond MIR laser source, which is tunable in a wide wavelength range (3-8 $\mu$m) and with adjustable spectral bandwidth.

## 1.2 THE ROUTES TO ULTRAFAST MIR SOURCES

There are many direct ways to generate MIR sources, such as a $CO_2$ laser, a quantum cascade laser (QCL) as well as solid-state media doped with $Cr^{2+}/Fe^{3+}$ or Ho/Tm. These types of lasers are widely applied in laser manufacturing, optical communication, and laser sensing [9–11]. However, they can not achieve either high-intensity output or wide wavelength tunability, which is often required for various applications. $CO_2$ lasers can work in the continuous-wave (CW) mode or the pulsed-mode, with the shortest pulse widths of the order of picoseconds. Besides, its wavelength tunability is limited[12, 13]. QCLs are mainly constrained by their pulse's energies (typically pJ/nJ-level). Although doped solid-state lasers can produce mJ-level femtosecond pulses, the wavelength of the output is confined to the short-wave infrared (SWIR) region, typically <4 $\mu$m [14, 15].

Due to the lack of proper active gain media for the direct generation of laser pulses in the mid-wave infrared (MWIR) range (i.e. 4-8 $\mu$m) by stimulated emission, parametric nonlinear frequency conversion is a promising approach to generate MWIR pulses. Based on DFG or OPA, researchers have developed either Ti:Sapphire or Yb-based drivers with mJ energies at kHz repetition rates for parametric amplification architectures.

From Figure 1.1, it is apparent that it is rare for Ti: Sapphire-driven OPA/OPCPA systems to efficiently generate high-energy output for wavelengths above 4 $\mu$m. Although Ti: Sapphire CPA laser sources are able to deliver stable millijoule-to-joule-level (depending on the repetition rate) ultrashort ($\sim$ 30 fs) pulses, the frequency gap between the driving laser and the aimed idler output in the MIR region is so large that intermediate frequency conversion stages are required, increasing the complexity of the laser architecture. Furthermore, constraints from the nonlinear crystals pumped at 800 nm, such as limited transparency, two-photon absorption, and narrow phase-matching bandwidth are also often difficult to deal with.

The other common driving sources are $Yb^{3+}$ or $Nd^{3+}$ doped CPA systems centred at 1.03 $\mu$m or 1.06 $\mu$m. Commercial 1-$\mu$m CPA systems can generate pulses with multi-mJ energies and pi-

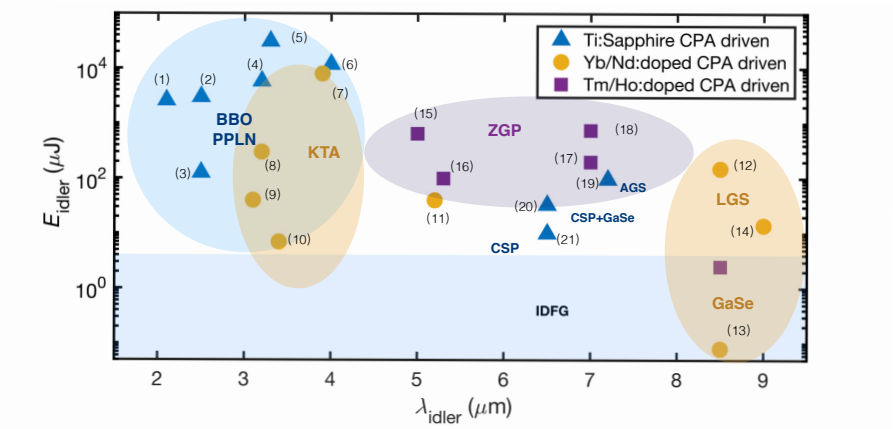


Figure 1.1: Conclusion of different driving lasers for generation of ultrashort MIR laser pulses.
BBO/PPLN-based OPA/OPCPA driven by Ti:Sapphire CPA (1)-(6):[14, 16–20];
KTA-based OPA/OPCPA driven by Yb/Nd-doped CPA (7)-(10):[21–24];
ZGP-based OPA/OPCPA driven by Tm/Ho-doped CPA(11),(15)-(18):[25],[26–29];
AGS,CSP,GaSe-based OPA/OPCPA driven by Ti:Sapphire CPA (19)-(21):[30–32];
LGS/GaSe-based OPA/OPCPA driven by Yb-doped CPA (12)-(14):[33–35].

cosecond pulse durations. OPA/OPCPA systems driven by 1-$\mu$m CPAs have good spectral coverage in SWIR and LWIR, but the energy of the idler is typically limited to 100 $\mu$J, which indicates that more pump energy from the front-end driver is necessary.

In the past few years, the development of high-energy ultrafast MIR sources through OPA/OPCPA has been extended towards MWIR and LWIR. It benefits from the exploitation of various non-oxide crystals, which are transparent in this wavelength regime, and have impressively high nonlinearities in MWIR, such as ZGP, CSP, and AGS [30–32, 36]. This has also been made possible due to the development of novel pump laser sources at 2 $\mu$m [25, 28, 36–39]. Crystals such as AGS and CSP have relatively low damage threshold, while the transparency of ZGP (2-8.5 $\mu$m) dictates the wavelength of the pump laser to be above 2 $\mu$m. In order to gain higher output energy in the MWIR, novel ultrashort 2-$\mu$m pumping sources are desired. Pumping with 2-$\mu$m lasers, not only can

it allow nonlinear crystals to achieve broader phase-matching bandwidths, but it can also endure higher pump intensity [40]. The demand for high-intensity ultrashort laser pulses at 2 $\mu$m has stimulated the recent development of various 2-$\mu$m CPA systems. A few groups have developed mJ-level, ps-scale, 2-$\mu$m Ho:YLF-based or Ho:YAG-based regenerative amplifiers. Further cascade CPA stages, such as booster amplifiers, have also been built to enhance the output energy up to a few tens of mJ [41, 42] or even 270 mJ under cryogenic conditions [36]. With the help of powerful 2-$\mu$m picosecond pumps, combined with large-aperture highly nonlinear ZGP crystals, a-few-cycle mJ-level output in the MWIR range is expected in the near future, which will be a promising driving source for various applications. Although 2-$\mu$m CPA systems have allowed impressive performances of high-intensity 100fs-scale OPAs/OPCPAs, the laser architecture of often rather complex. Moreover, all current ultrafast MWIR OPA/OPCPA systems are specialized in acquiring few-cycle intense laser pulses at one particular MWIR wavelength, typically for applications in strong-field or attosecond physics. The wavelength tunability of these laser sources in the MIR range (typically 3 - 8 $\mu$m), where various vibrational excitation modes are located, is not flexible enough for various spectroscopic applications. These experiments often rely on the effortless tuning across the molecular fingerprint regime and adjusting the spectral bandwidth for either mode-selective vibrational excitation or concurrent excitation of multiple key vibrational modes for 2D-IR spectroscopy. Although the potential of novel ZGP-based OPA/OPCPAs has been previously demonstrated, this thesis reports a compact OPA/OPCPA laser source readily tunable in the molecular fingerprint regime (typically 3-8 $\mu$m).

## 1.3 OBJECTIVES AND STRUCTURE OF THIS THESIS

The objective of this thesis is the realization of a compact OPA system, which is easily tunable in the molecular fingerprint regime (3-8 $\mu$m).

The structure of this thesis is summarised below:

*Chapter 2* focusses on the seed generation for DFG/OPA from the transform-limited 2-$\mu$m, 3-ps output of our home-built Ho:YLF regenerative amplifier via SC generation in bulk media. Comparison of SC generation in YAG, ZnSe, and GaAs is also presented.

*Chapter 3* presents the design and simulations of optical parametric amplification in ZGP. Because of the high nonlinearity of the ZGP crystal, back conversion is taken into consideration. OPA processes are simulated under different crystal lengths as well as different spatial and temporal overlap ratios of the signal and the pump.

*Chapter 4* demonstrates the construction and characterization of the ZGP-based OPAs in the molecular fingerprint regime seeded with SC based on YAG and ZnSe crystal.

*Chapter 5* summarizes the accomplished work.

## 1.4 Contributions of this thesis

*Multi-octave SC generation in bulk media pumped with multi-picosecond 2-$\mu$m laser pulses*

We resolve the issue of detrimental damage induced by avalanche ionization due to multi-picosecond MIR driver laser pulses. By applying a loosely-focussing pumping geometry onto the long bulk crystal, we obtain multi-octave SC from 500 nm to 4.5 $\mu$m in 15cm-long YAG crystal. In addition, we also compare characteristics of SC generated in YAG, ZnSe, and GaAs crystals under identical pumping conditions.

*$ZnGeP_2$-based optical parametric amplifiers*

We build a compact setup with parallel lines of cascaded ZGP-based OPAs, which can be independently tunable in the molecular fingerprint regime (3-8 $\mu$m). The compressibility of the idler is demonstrated by inserting a Ge bulk crystal to compensate for dispersion.

*Diagnostic setup for ultrashort MIR pulses*

We also construct a SHG-frequency-resolved optical gating (FROG) setup for the characterization of the ultrashort MIR laser pulses. By selecting suitable thin nonlinear crystals (BBO, AGS, GaSe) and appropriate spectrometers, ultrashort laser pulses within 2-8 $\mu$m can be characterized.

# 2

# SUPERCONTINUUM GENERATION DRIVEN WITH 3-PICOSECOND 2-$\mu$m PULSES

SC generation in bulk media is a complicated interplay between nonlinear optical processes, such as self focusing (SF), self phase modulation (SPM), and other complicated plasma generation processes. Alfano and Shapiro first discovered SC generation in a borosilicate glass sample with a picosecond Nd-glass mode-locked laser source, ranging from the visible to the near infrared [43].

Although the first experiment of SC generation in bulk media was conducted with a picosecond laser source, SC generation in bulk media is at present often carried out and discussed in the context of femtosecond laser pumping sources. This is due to the rapid progress in the development of stable and intense femtosecond laser sources spurred by the invention of the chirped pulse amplification (CPA) technique, which avoids the irreversible damage of the laser media while drastically increasing the pulse energy. SC generation in bulk media with the aid of mature femtosecond laser sources, in turn, promotes the development of femtosecond OPCPA or OPA. SC-seeded OPCPA/OPA can generate a widely-tunable idler output with passively-stabilized carrier-envelope phase (CEP) [44], which is vital in frequency comb metrology and attosecond physics [45, 46].

Recently, the development of high-energy, ultrafast OPCPA/OPA in the MIR regime, has encountered difficulty in SC generation, when driven directly by multi-ps high energy RAs, due to the high probability of damaging the bulk media. Researchers have bypassed the obstacle through either DFG from the femtosecond oscillator [28, 41], with the assistance of the intermediate second-harmonic-pumped SC-seeded OPA stages[25], or Kagome-fiber-based pulse compression techniques[47]. However, these alternative approaches introduce considerable additional complexity to the system or rely on exacting fabrication constraints. The necessity of SC generation powered by multi-ps MIR pulses in bulk

media has prompted us to delve into the essential underlying mechanisms.

## 2.1 Mechanisms of SC generation in bulk media

One evident phenomenon associated with SC generation in bulk media is a luminescent track inside, namely a "filament", arising from the sustainable interplay between temporal and spatial Kerr effects and photoionization under certain conditions over a long distance. In the following section, two main important mechanisms under the dynamics, Kerr effect, and photoionization, are briefly introduced.

### 2.1.1 *Self focusing and self phase modulation*

Nonlinear optical effects are described as the nonlinear response of the optical characteristics of the material by the applied optical field, and the optical responses are elucidated by the polarization **P**, defined as the dipole moment per volume of the substance,

$$\mathbf{P} = \epsilon_0 \left[ \chi^{(1)}\mathbf{E} + \chi^{(2)}\mathbf{E}^2 + \chi^{(3)}\mathbf{E}^3 + \cdots \right] \tag{2.1}$$

with $\epsilon_0 = 8.854 \times 10^{-12}$ F/m the vacuum dielectric constant, and $\chi^{(i)}$ the susceptibilities. Apart from the linear susceptibility $\chi^{(1)}$, $\chi^{(2)}$ and $\chi^{(3)}$ are responsible for the second- and third-order nonlinear polarizations ($\mathbf{P}^{(2)} = \epsilon_0\chi^{(2)}\mathbf{E}^2$ and $\mathbf{P}^{(3)} = \epsilon_0\chi^{(3)}\mathbf{E}^3$ ), respectively. The third-order nonlinearity accounts for the quadratic response of the refractive index with respect to the optical field, which is also named the **Kerr effect**, expressed as follows:

$$n = n_0(\omega) + n_2 I = n_0(\omega) + \frac{3}{2}\frac{\chi^{(3)}|E|^2}{n_0} \tag{2.2}$$

On the one hand, SF is the spatial Kerr effect in the transverse direction, which is also called **Kerr focusing**. As an intense Gaussian beam is focused on the bulk medium, the optical electrical field transversely modulates the refractive index of the medium, locally transforming the bulk medium into a "Kerr" focal lens, which spatially focuses the input pulses. This effect leads to the

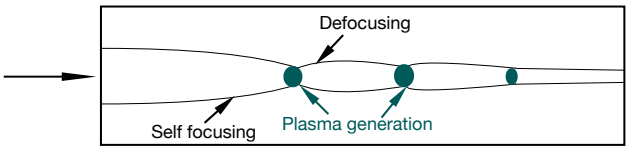


Figure 2.1: Illustration of the formation of filament in bulk medium.

increase of the local optical intensity, exceeding the threshold of electron ionization.

To trigger SF in bulk medium, the input power is required to exceed a critical threshold, known as the **critical power**. For a Gaussian beam, the critical power is defined as follows:

$$P_{cr} = \frac{2.72\lambda^2}{8\pi n_0 n_2} \tag{2.3}$$

On the other hand, SPM is the temporal/longitudinal Kerr effect. The time-dependent variation of the refractive index creates a corresponding time-dependent change in the phase of the pulse, represented as follows:

$$\phi_{nl}(t) = \frac{\omega_0}{c} n_2 I(t) z, \tag{2.4}$$

where $n_2$ is the nonlinear refractive index, $\omega_0$ is the input central frequency, and $z$ is the distance along the propagating direction. The time-varying change in the refractive index induces the instantaneous frequency

$$\omega(t) = \omega_0 + \Delta\omega(t) = \omega_0 - \frac{\partial}{\partial t}\phi_{nl}(t), \tag{2.5}$$

$$\Delta\omega(t) = 2\frac{\omega_0 z}{c{\tau_p}^2} n_2 I_0 \exp\left(-\frac{t^2}{\tau_p^2}\right) \cdot t, \tag{2.6}$$

where $\tau_p$ is the duration of the input Gaussian pulse. As indicated in (2.6), for a Gaussian laser pulse, the time-varying modulation on the phase of the pulse will give rise to a red-shift ($\Delta\omega(t) < 0$) in the leading part of the pulse, and a blue-shift ($\Delta\omega(t) > 0$) in the rear part.

### 2.1.2 *Plasma generation*

Due to the self-focusing effect, the electrons ionized from the matter are formed into plasma, lowering the refractive index in the core of the beam and defocusing the beam as a concave lens. This negative modification in the refractive index is approximated according to the Drude model as follows:

$$\Delta n_e = -\frac{2\pi e^2 \rho_e}{n_0 m_e(\omega_0^2 + \nu_e^2)}, \tag{2.7}$$

where $\rho_e$ is the electron density, and $\omega_0$ and $\nu_e$ are the laser frequency and electron collision frequency, respectively. Here, $\nu_e$ is related to the collision time, $\tau_c$. As $\rho_e$ grows up to the level of $10^{17} cm^{-3}$, $n_2 I$ in (2.2) will be compensated due to the free electrons. Photoionization (PI) is the phenomenon describing the electron excitation from the valence band to the conduction band because of photon absorption. Depending on the input optical intensity, the PI process may involve three different mechanisms, i.e. tunneling ionization (TI), multiphoton ionization (MPI), and avalanche ionization (AI). Keldysh derived a formula, also called the Keldysh parameter. It differentiates the three mechanisms mentioned above and is given as [48]

$$\gamma = \frac{\omega}{e}\sqrt{\frac{m c n_0 \varepsilon_0 E_g}{I}} \tag{2.8}$$

where $\omega$ is the frequency of input pulses, $e$ is the charge of the electron, $m$ is the reduced effective electron-hole mass, $c$ is the speed of light, and $n_0$ is the refractive index at frequency $\omega$. $E_g$, $\varepsilon_o$ and $I$ are the bandgap energy of the medium, the free-space permittivity, and the local intensity of the input pulse, respectively.

| Keldysh parameter $\gamma$ | | |
|---|---|---|
| $\ll$1.0 | $\backsim$ 1.0 | $\gg$1.0 |
| TI | TI, MPI | MPI |

The MPI rate is given by:

$$W_{\mathrm{MPI}} = \sigma_N I^N \tag{2.9}$$

where $W_{\mathrm{MPI}}$ is the MPI rate, and $N$ is the number of photons sufficient to free one electron, given by $N = \mathrm{mod}(U_i/\hbar\omega) + 1$. $\sigma_N$ is the ionization coefficient of MPI. In SC generation with femtosecond pulses, the main plasma generation mechanism is due to MPI. The MPI rate is presented in Keldysh theory in a condensed matter as (2.9).

In contrast with MPI, AI is the process in which free electrons excited by previous MPI process obtain kinetic energy ($\geq E_g$) by absorption of additional multiple photons, increasing the probability for collisional ionization of neighboring atoms to generate free electrons. As presented in (2.10) [49, 50], the ionization rate linearly depends on the input intensity. Once the intensity is sufficient to support AI, the long pulse duration facilitates the rapid growth of free electrons through the AI process, which might produce excessive electrons beyond the critical electron density, leading to permanent damage of the crystal. The AI rate is given as

$$W_{\mathrm{AI}} = \frac{\sigma_{\mathrm{IB}} I}{U_{\mathrm{i}}}, \tag{2.10}$$

where the electron collision rate $\sigma_{\mathrm{IB}}$ is also called the inverse Bremsstrahlung coefficient, derived from the electron collision time $\tau_c$, as shown in (2.11).

$$\sigma_{\mathrm{IB}} = \frac{e^2}{\epsilon_0 m_e c n_0} \frac{\tau_c}{(1 + \omega^2 {\tau_c}^2)} \tag{2.11}$$

### 2.1.3 *Second-harmonic generation and third-harmonic generation*

SHG is a typical $\chi^{(2)}$ process, which doubles the fundamental frequency as the phase of the two beams is matched. It only occurs in noncentrosymmetric nonlinear media, but it still exerts an influence on SC generation through so-called second-order cascading in materials possessing both $\chi^{(2)}$ and $\chi^{(3)}$ nonlinearities, such as PPLN and $\beta$-BBO [51, 52]. The frequency component of the second-order polarization is depicted below:

$$P(2\omega) = \epsilon_0 \chi^{(2)} E(\omega)^2 \tag{2.12}$$

In addition to SC generation, SHG is also exploited as a tool to characterize ultrashort pulses, such as SHG-FROG. Details about SHG-FROG setup are included in Appendix A.

Besides SHG, a $\chi^{(2)}$ process that can only be observed in non-centrosymmetric media, a $\chi^{(3)}$ process, which could appear in both centrosymmetric and noncentrosymmetric media, is third-harmonic generation (THG). In the context of SC generation, apart from SPM, normally THG produces a prominent third harmonic spectral component at the blue side of the overall SC spectrum. The responsible third-order polarization for THG is expressed below:

$$P(3\omega) = \epsilon_0 \chi^{(3)} E(\omega)^3. \tag{2.13}$$

## 2.2 THE DILEMMA FOR MULTI-PICOSECOND MIR PUMPING SOURCE

As mentioned above, extensive research has been conducted in bulk media, pumped with femtosecond laser pulses ranging from 800 nm to 1 $\mu$m [53]. The critical-power criterion implied in (2.3) is often trivially satisfied for most femtosecond applications [50, 54]. However, SC generation in bulk media with multi-ps or even longer pulses at longer wavelengths ( >1.5 $\mu$m) becomes rather challenging, because it poses severe constraints due to the wavelength-scaling of the critical power criterion and the propensity to induce avalanche-ionization-seeded breakdown mechanisms, as revealed in equations (2.3) and (2.10).

Although a few experiments of SC generation with picosecond or nanosecond laser pulses have been tested in sapphire, YAG [55, 56], ZnSe [57, 58], and GaAs [59], the underlying cause for the damage and solutions to it are not well-understood.

## 2.3 AVOIDING DAMAGE

Bulk media for SC generation vary from dielectrics and semiconductors. They own high nonlinearity, wide transparency windows (typically spanning from the visible to the deep MIR region), as well as large bandgap, which facilitates extending the blue-shifted

cut-off wavelength into the visible region. A few key parameters of commonly used bulk media for SC generation in the MIR range are listed below in table 2.1.

| Material | $U_g$(eV) | Transmission window ($\mu$m) | $n_2 \times 10^{-16} cm^2/W$ | $\lambda_{ZDW}(\mu m)$ | $P_{cr}(MW)@2\mu m$ | $F_{th}(J/cm^2)$ |
|---|---|---|---|---|---|---|
| YAG | 6.5 | 0.21-5.2 | 6.2 at 2$\mu$m | 1.6 | 4.1 | 7.5 (500fs, at 1.03$\mu$m) |
| Sapphire | 9.9 | 0.19-5.2 | 2.9 | 1.31 | 5.36 (500fs, at 1.03$\mu$m) | - |
| ZnSe | 2.71 | 0.5-20 | 60, 300 | 4.8 | 0.31 | - |
| GaAs | 1.42 | 0.9-17.3 | 300, 3300 | 6.0 | 0.045 | 0.119 ( 2$\mu$ m, 3 ps)* |

Table 2.1: Parameters for typical dielectric media and semiconductors; $U_g$:bandgap energy; $n_2$: nonlinear refractive index; $\lambda_{ZDW}$: zero dispersion wavelength, all data are collected from [54, 60], *: experimental result described in this thesis.

For example, in YAG, to estimate the intensity threshold for arresting optical breakdown, the evolution of the electron density, $\rho(t)$, as a function of the laser intensity, $I$, may be approximated by a simplistic model [50, 54, 61] that incorporates avalanche ionization, seeded by optical field ionization, and governed by the equation:

$$\frac{\partial \rho}{\partial t} = W_{\mathrm{OFI}}(I)(\rho_{nt} - \rho) + W_{\mathrm{AI}}(I)\rho \tag{2.14}$$

where $\rho_0$ denotes the background neutral density. The optical-field-ionization rate, $W_{\mathrm{OFI}}$, may be evaluated following the Keldysh formulation [62, 63], as shown in Figure 2.2a for YAG with a band gap energy of $U_{\mathrm{i}} = 6.5$ eV [64, 65] and $\lambda = 2.05$ $\mu$m. The low-intensity ($< 10^{12}$ W/cm$^2$) asymptote corresponds to a multiphoton-ionization rate, given by $W_{\mathrm{MPI}} = \sigma_{11} I^{11}$, where $\sigma_{11} = 1.3 \times 10^{-126}$ s$^{-1}$ (W/cm$^2$)$^{-11}$ for $\rho_0 = 7 \times 10^{22}$ cm$^{-3}$ [65]. The rate of avalanche ionization, on the other hand, may be expressed as $W_{\mathrm{AI}} = \sigma_{\mathrm{IB}} I / U_{\mathrm{i}}$, according to the Drude model, where an estimated collision time, $\tau_c = 3$ fs [65], yields an inverse Bremsstrahlung coefficient of $\sigma_{\mathrm{IB}} = 2.06 \times 10^{-17}$ cm$^2$. The simulation results are illustrated in Figure 2.2b, which shows that beyond a threshold intensity of $I_{\mathrm{th}} \sim 3 \times 10^{11}$ W/cm$^2$, the electron density, $\rho(t)$, rapidly reaches the plasma critical density, $\rho_c = 2.6 \times 10^{20}$ cm$^{-3}$, for the duration of our pump pulse, resulting in significant plasma absorption and potential irreversible material damage. Consequently, stable SC generation at $\sim 10 P_{\mathrm{cr}}$

with an intensity $\lesssim 10^{11}$ W/cm$^2$ to avoid damage dictates a focusing geometry with a numerical aperture (NA) $\lesssim 0.005$, which motivated the design of the experimental setup. Therefore, a simple experimental geometry is constructed, relying on a very low numerical aperture [66] for the pump pulse and a crystal length commensurate with the Rayleigh length of the focusing geometry.

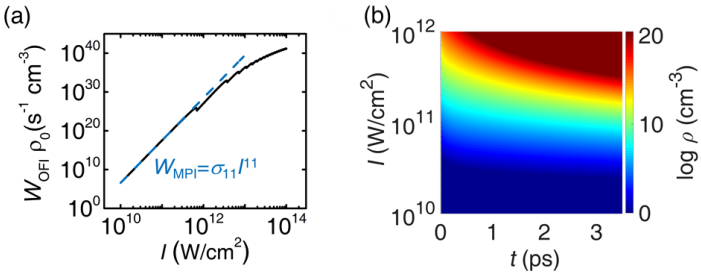


Figure 2.2: (a) Calculation of the optical-field-ionization rate, $W_{\mathrm{OFI}}$, as a function of the intensity, $I$, for YAG with a laser of central wavelength, $\lambda = 2.05$ $\mu$m, where $\rho_0$ denotes the background neutral density. The low-intensity asymptote corresponds to a multiphoton-ionization rate, $W_{\mathrm{MPI}} = \sigma_{11} I^{11}$. (b) Simulation of the evolution of the plasma density, $\rho(t)$, as a function of $I$ for the duration of the pump pulse [67].

## 2.4 INFLUENCE OF GROUP VELOCITY DISPERSION

### 2.4.1 *Anomalous dispersion regime*

When the pump is located within the anomalous dispersion regime, nonlinearity, anomalous dispersion, and plasma generation will have intertwined effects on the pump, forming a typical spatiotemporally localized wavepacket, named a *light bullet*. The 'bullet' can have a huge impact on the frequency domain, creating a super broad spectrum, which may span over a few octaves.

#### 2.4.1.1 *SC generation in YAG*

As indicated in Tab. 2.1, the zero dispersion wavelength of YAG lies around 1.6 $\mu$m. Thus, we will investigate SC generation in YAG within the anomalous dispersion regime, by utilizing a

home-built 2$\mu$m 3-ps Ho:YLF regenerative amplifier. The resulting SC ranges from 500 nm to 3.5 $\mu$m (measured at -30 dB with spectral components at wavelengths up to 4.5 $\mu$m). Its corresponding dynamics of filament formation in this interaction regime are inspected by monitoring the spectral and temporal evolution of the pulse during its propagation through the length of the crystal.

Recently, SC generation in a 13-cm long YAG crystal, pumped in the normal dispersion regime by a chirped, 1-$\mu$m, 3-ps pump pulse (with a transform limit of 1.8 ps) was reported [68], although the measurements were confined only to the blue, anti-Stokes continuum (500 – 950 nm) and it was not *a priori* apparent why long focal and crystal lengths produce stable SC with ps pulses [69].

Here, stable multi-octave SC generation is demonstrated supported even by the 2-nm bandwidth of a 3-ps pump pulse centered at 2.05 $\mu$m (corresponding to a transform limit of 1.8 ps), despite a four-fold increase in the critical power requirement due to the wavelength-scaling. We present the multi-octave SC spectrum, ranging from the visible ($\gtrsim$ 500 nm) to the MIR ($\lesssim$ 4.5 $\mu$m ), along with its energy-dependence as well as long-term stability, and probe the evolution of the pulse propagating through the length of the crystal in the spectral and temporal domains.

The output of our Ho:YLF regenerative amplifier [37], operated at a repetition rate of 1 kHz, was focused into a YAG crystal with NA varying in the range 0.001 – 0.005. Different combinations of crystal length (5 cm, 10 cm, and 15 cm) and focal length for the pump beam (50 cm, 75 cm, and 100 cm) were used to optimize the spectral extent of the SC generation, with further optimization of the numerical aperture of the pump beam performed by an adjustable iris. The position of the YAG crystal along with the laser propagation axis was also optimized and the pump energy was varied by a combination of a thin-film-polarizer and a half-waveplate. A crystal length of 15 cm and a pump numerical aperture of $\sim$ 0.005, corresponding to a Rayleigh length of $\sim$ 12 cm, were found to produce the most optimum SC (in terms of bandwidth and stability). A long, stable, single filament was observed in the bulk of the YAG crystal (as shown in Figure 2.6),

along with the characteristic conical emission of colored rings in the visible, resembling typical SC generation from femtosecond sources. The filament formation was initiated at the rear end of the 15-cm YAG crystal for pump energy of $\sim$ 17 $\mu$J and was found to shift towards the front end of the crystal on increasing the pump energy until $\sim$ 175 $\mu$J, which was determined as the threshold for irreversible crystal damage. At this energy, the filament started $\sim$ 5 cm from the front end of the crystal.

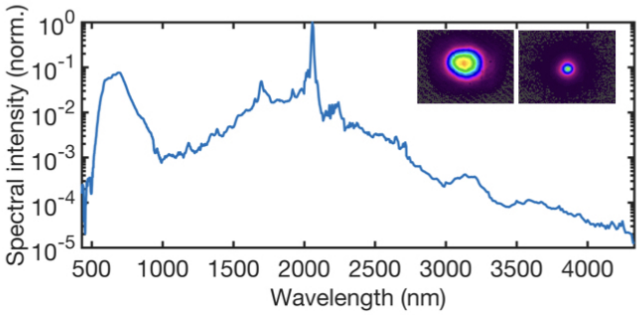


Figure 2.3: The spectral extent of the SC generated in a 15-cm YAG crystal for pump energy of 150 $\mu$J and NA $\sim$ 0.005. The inset shows the spatial profile of the pump beam (left) and the SC output (right) in the far field [67].

Figure 2.3 shows the spectral extent of the SC generated, when pumped at 150 $\mu$J, measured with a series of spectrometers in the spectral ranges 200-1100 nm, 1000-2000 nm, and 900-2500 nm, respectively, and a monochromator, coupled to a liquid-nitrogen-cooled MCT detector for the wavelength range 2400-4300 nm. Multiple short-pass and long-pass filters were used to eliminate the residual pump, when necessary, and enhance the dynamic range of the spectral measurements. Scaling factors, derived from the overlapping spectral regions from the different spectrometers, were then applied. Figure 2.3a shows the residual pump at 2.05 $\mu$m, along with a cascaded SC triggered by the third harmonic at $\sim$ 686 nm [70], as well as Raman Stokes' peaks in the range 2100-2250 nm and weak anti-Stokes' peaks at $\sim$ 1950 nm.

A 2.4-$\mu$m longpass filter and a 1-$\mu$m shortpass filter were used to eliminate the residual pump (to prevent saturation of the spectrometers) and monitor the dependence of the spectral intensity in the visible and near-infrared (vis-NIR) and the MIR as a function of the pump energy, $E_p$, as shown in Figure 2.4a and 2.4b

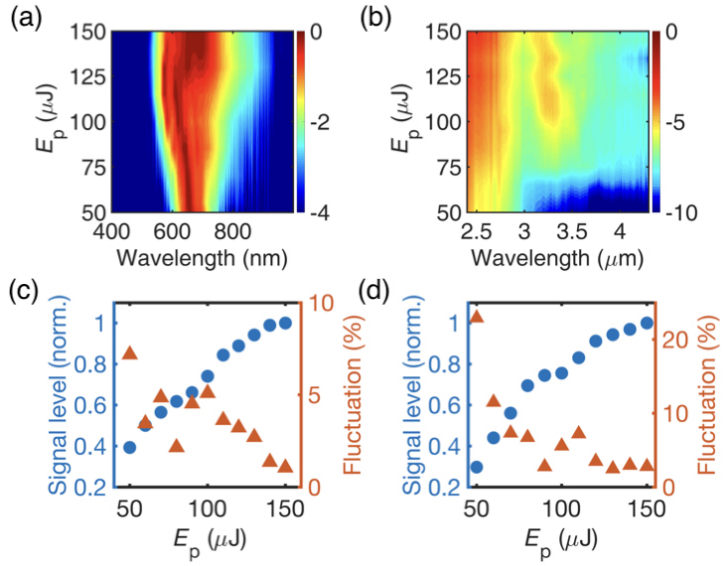


Figure 2.4: (a) Self-normalized spectral intensity in logarithmic scale (indicated by the colorbar) as a function of the pump energy, $E_p$, in the vis-NIR and MIR, respectively. (b, c) Scaling of the spectral intensity integrated over wavelength as well as the standard-deviation fluctuation for vis-NIR and MIR, respectively, as a function of $E_p$ [67].

respectively. The difference in the dynamic range of the spectral intensity between the measurements in the vis-NIR and MIR is owing to the disparate sensitivities of the Si and MCT detectors used. The corresponding scaling of the spectral intensity, integrated over wavelength, with respect to the pump energy, $E_p$, is shown in Figure 2.4(c) and 2.4(d) respectively, along with the standard-deviation fluctuations, and were corroborated by independent measurements with photodiodes. The fluctuations, measured for 5 minutes at a repetition rate of 1 kHz, clearly show a decreasing trend with increasing pump energy, as expected, for the vis-NIR. The energy efficiency of the SC generation, including the residual pump energy, was estimated to be $> 60\%$, with $\sim 1$ $\mu$J of the energy above 2.4 $\mu$m, when pumped at 120 $\mu$J.

Figure 2.5 presents the long-term stability of the SC spectrum over a period of 20 minutes at a repetition rate of 1 kHz for pump energies of 150 $\mu$J (for vis-NIR) and 130 $\mu$J (for MIR), in accordance with the minimum-fluctuation points in Figure 2.4c and 2.4d, respectively. The standard deviation of the fluctuations was

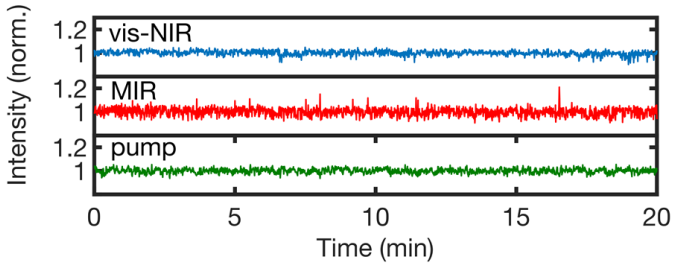


Figure 2.5: Long-term stability of the SC spectrum in the vis-NIR and MIR, as well as the pump, for 20 minutes at a repetition rate of 1 kHz for pump energies of 150 $\mu$J and 130 $\mu$J (from Figure 2.4), respectively. The standard deviation of the fluctuations of the vis-NIR as well as the MIR was found to be 1.9 %, which is the same as that of the pump [67].

measured to be 1.9% for both the vis-NIR and the MIR, which is the same as that of the pump.

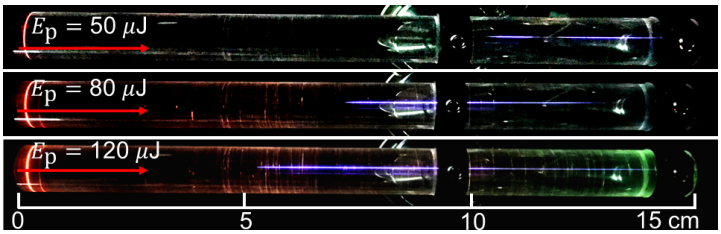


Figure 2.6: Filaments pumped at 50 $\mu$J, 80 $\mu$J, and 120 $\mu$J in a 15-cm long crystal [67].

Figure 2.6 illustrates the filament formation for various pump energies, clearly depicting the varying distance $L$, where the filament starts from the front (input) end of the 15-cm long crystal. To understand the dynamics of the temporal pulse profile in the course of its propagation through the length of the crystal, we performed second-harmonic-generation-based frequency-resolved-optical-gating (SHG-FROG) measurements of the SC output for various crystal lengths and pump energies.

Figure 2.7 illustrates the pulse characteristics of the output of our Ho:YLF regenerative amplifier used to pump the SC-generation stage, showing a pulsewidth (FWHM) of 3.0 ps. For $E_p \sim 50$ $\mu$J, corresponding to $L \sim 10$ cm, an SHG-FROG measurement of the output of a 5-cm long crystal (where no filament is formed) shows a nearly unperturbed temporal profile, remarkably similar to the pump profile. For a 10-cm crystal, however, this pump en-

ergy corresponds to the brink of filament formation, and both the spectral and the temporal profiles were found to exhibit strong self-phase-modulation (SPM). This effect is further augmented in a 15-cm long crystal, where a ~ 5-cm long filament is formed at this pump energy, and the pulse splits into a train of multiple "pulselets" in the temporal domain.

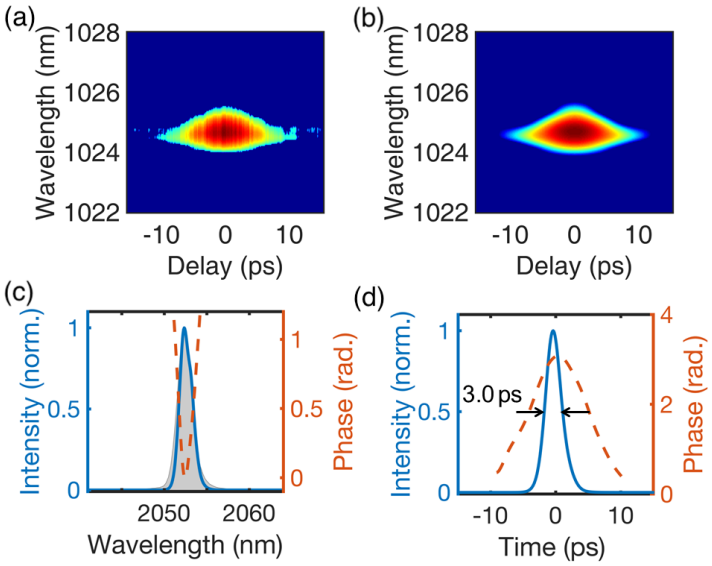


Figure 2.7: SHG-FROG measurement of the pump pulse. (a, b) Self-normalized measured and retrieved FROG profiles in the logarithmic scale, respectively. (c) Measured (gray shaded area) and retrieved (blue solid line) spectra along with the spectral phase (red dotted line). (d) Retrieved temporal profile (blue solid line), with a pulsewidth of 3.0 ps (FWHM), along with the temporal phase (red dotted line). The retrieval error is 0.3% [67].

Figure 2.8 illustrates a representative scenario for a 10-cm long YAG crystal at $E_p \sim 80\ \mu$J, where filament formation has been initiated at the rear end of the crystal and the pulse splits into multiple pulselets of duration ~ 1 ps. Similar observations were also made by measuring the SHG-FROG of the output from a 15-cm long crystal with varying pump energies. Below the threshold for filament formation, the pulse profile starts exhibiting signatures of SPM, which are further magnified on increasing the pump energy until at $E_p \sim 120\ \mu$J, when the filament is ~ 10 cm long, the output shows a strongly modulated spectrum, along with a distinct single peak in the temporal domain with a

pulsewidth (FWHM) of ~ 350 fs, coupled with a pedestal that displays various SPM-generated non-linear effects, particularly self-steepening. Interestingly, similar pulse-splitting effects have previously been observed in SC generation with a 6.7-cm long GaAs crystal, when pumped by a pulse-train of 3-ps pulses from a $CO_2$ laser at a central wavelength of 10.6 $\mu$m [71].

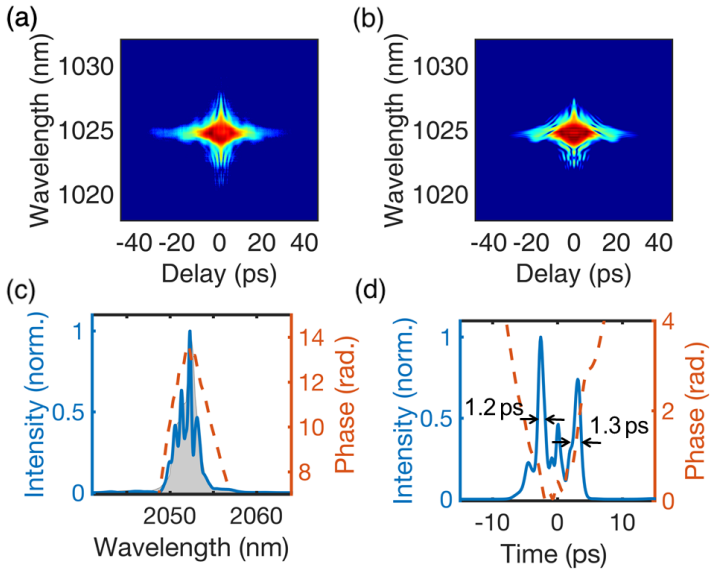


Figure 2.8: SHG-FROG measurement of the output of a 10-cm long YAG crystal pumped at 80 $\mu$J, where filament formation has already been initiated at the rear end of the crystal. (a, b) Self-normalized measured and retrieved FROG profiles in the logarithmic scale, respectively. (c) Measured (gray shaded area) and retrieved (blue solid line) spectra along with the spectral phase (red dotted line). (d) Retrieved temporal profile (blue solid line), along with the temporal phase (red dotted line). The retrieval error is 0.9%. [67]

Although SC generation in anomalous dispersion regime enables pumping with long pulses with broader and higher spectral intensity, due to the self-compression mechanism, it still struggles with deterioration in spectral coherence and stability. Degradation of the spectral coherence has been discussed in the context of SC generation in the anomalous dispersion regime inside a fiber [72]. It is attributed to the so-called modulation instability (MI). MI originates from the amplification of random perturbations in the amplitude of the pumping field. Therefore, on one hand, SC coherence is contaminated by the amplified random noise; on

the other hand, the long-duration pulse is easily split by the amplified perturbation, which results in a more complex temporal profile [73], enhancing the instability of SC. With regard to SC generation in bulk YAG driven with 3-ps 2$\mu$m laser pulses, the propensity to evoke MI is observed in our experiments as well.

In summary, a generic recipe for circumventing avalanche-ionization-induced breakdown mechanisms is presented, while triggering high-energy, multi-octave, stable SC generation in bulk media with 2-$\mu$m, multi-ps pulses. However, coherence and stability of SC are critically important to the compressibility and stable performance of the subsequent OPCPA/OPA stages. Thus, we next resorted to SC generation in the normal dispersion regime in semiconductors.

### 2.4.2 *Normal dispersion regime*

In contrast to SC in anomalous dispersion regime, SC generation in the normal dispersion regime behaves differently in temporal and spectral domains. SPM creates a red-shifted spectral component at the leading part of the pulse and a blue-shifted spectral component at the rear part. The broadened SC then travels in the normal dispersion regime, where the red-shifted component travels faster compared to the blue-shifted component. Consequently, the pulse is temporally split. Simultaneously, each split sub-pulse experiences a different velocity in the material owing to the intensity-dependent refractive index, which results in self steepening on each sub-pulse, dramatically enhancing the spectral broadening.

SC generation in the normal dispersion regime has been widely investigated by virtue of the availability of various ultrafast laser sources ranging from 800 nm to 1.5 $\mu$m. However, due to the lack of mature MIR laser sources at the moment, only a few low energy OPCPA systems or high-power $CO_2$ laser sources are used for MIR SC generation in some MIR-transparent semiconductors, such as ZnSe and GaAs in the normal dispersion regime or the anomalous dispersion regime [57, 59]. Semiconductors, as presented in Tab.2.1, possess significantly larger third-order nonlinearity, and broad transparency windows in the MIR re-

gion, which means that much lower energies are necessitated for attaining the critical power (CP), resulting in broader SC spectra. Recently, increasing attention has been drawn towards MIR SC generation, thanks to the recent development of high-power ultrafast MIR laser sources [74–76]. Nonetheless, MIR SC generation pumped with multi-ps MIR pulses has not yet been well studied.

#### 2.4.2.1 *SC generation in ZnSe*

Polycrystalline ZnSe has both excellent quadratic and cubic nonlinearities. It has been applied to ultrabroad MIR generation through intra-pulse difference-frequency generation pumped with few-cycle pulses at 1 or 2 $\mu$m [76] and high-harmonic generation[25, 29]. Moreover, as listed in Table 2.1, the $\chi^{(3)}$ coefficient of ZnSe is 2- to 3-order higher than that of YAG. It is expected to be an appropriate candidate for studying SC generation with bulk media in the normal dispersion regime.

We studied SC generation with 2-$\mu$m 3-ps laser pulses, utilized to pump SC generation in ZnSe with the same focusing geometry. The zero dispersion wavelength of ZnSe is located around 4.8 $\mu$m, enabling us to pump SC in the normal dispersion regime.

In Figure 2.9, the SC spectrum generated in a 15 cm-long ZnSe is presented, on pumping with 100 $\mu$J. Since the third harmonic at 684 nm is measured by a visible spectrometer with a relatively poor signal-to-noise ratio, the noise level in that region is erased but the peak intensity of the third harmonic is adjusted by the relative intensity compared to the second harmonic.

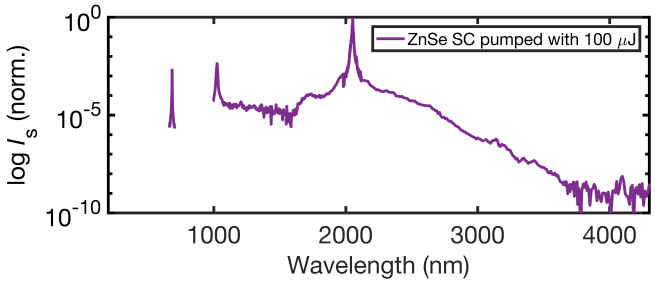


Figure 2.9: Overall SC spectrum from the visible region to the MIR region, on pumping with 100 $\mu$J in a 15cm-long ZnSe crystal.

The central part of the SC spectra around 2 $\mu$m on changing the pump energy, $E_p$, is shown in 2.10. The contour plot indicates the

dynamics of SC generation down to -30 dB. Spectral broadening appears when pumped with 2 $\mu$J (corresponding to $2P_{cr}$). SHG is observed simultaneously as the presence of the pump indicated in Figure 2.11 (c), the third harmonic shows up at around 2 $\mu$J. It is also important to mention that the weak SC spectra spreading beyond 2.1 $\mu$m are starting around 10 $\mu$J, but it is not apparent here because of the limited signal-to-noise ratio with this spectrometer for 2 $\mu$m. A more sensitive monochromator will reveal this, as in Figure 2.11 (a) and (b).

The red-shifted SC component ranging from 1.9 to 3.4 $\mu$m is separately presented in Figure 2.11 (a) and (b). In Figure 2.11 (c) and (d), the dynamics of the blue side of the SC spectra, including the third harmonic at 684 nm and a prominent second harmonic at 1026 nm are illustrated.

In summary, in contrast with YAG, SC generation in ZnSe displays a unique SPM-broadened multi-octave spectral pattern, mixed with second and third harmonics on the blue side. In the visible region, only a reddish core is observed due to the pulse intensity being diminished by the effect of dispersion and the diversion of energy into the second harmonic.

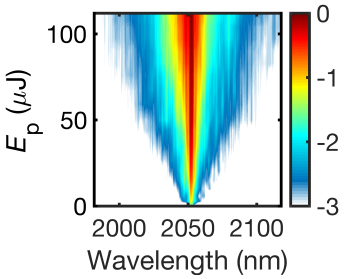


Figure 2.10: Evolution of normalized SC spectral intensity around 2 $\mu$m in logarithmic scale as a function of the pump energy in a 15 cm-long ZnSe crystal.

#### 2.4.2.2 *SC generation in GaAs*

Similar to ZnSe, GaAs is another potential candidate for SC generation. GaAs has even higher (1-4 times ) cubic nonlinearity than that of ZnSe. It has been systematically studied with femtosecond laser pulses both in the normal dispersion regime, near the zero dispersion wavelength, and the anomalous dispersion regime.

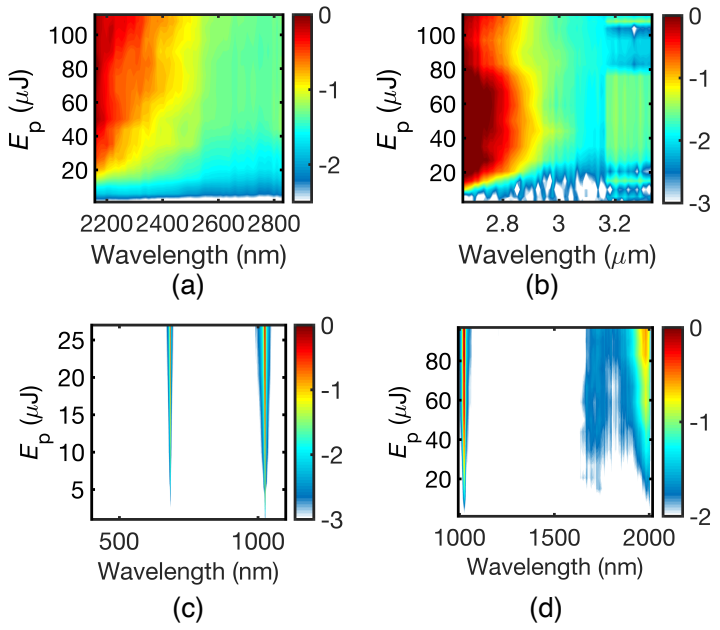


Figure 2.11: Evolution of the SC spectra varied with pump energy in the visible region and NIR region in a 15cm-long ZnSe crystal.

SC pumped with longer pulses was investigated in a ~ 7cm-long GaAs in anomalous dispersion regime pumped with multi-ps pulses (2.5 or 8 ps) at 9.3 $\mu$m [57] or a train of 3-ps pulses at 10 $\mu$m [59].

Although these investigations in GaAs have demonstrated its potential for SC generation in the MIR region, within the normal dispersion regime, SC generation in GaAs with multi-ps pulses has not yet been studied. In this section, SC generation in GaAs, driven by 3-ps 2-$\mu$m pulses is studied.

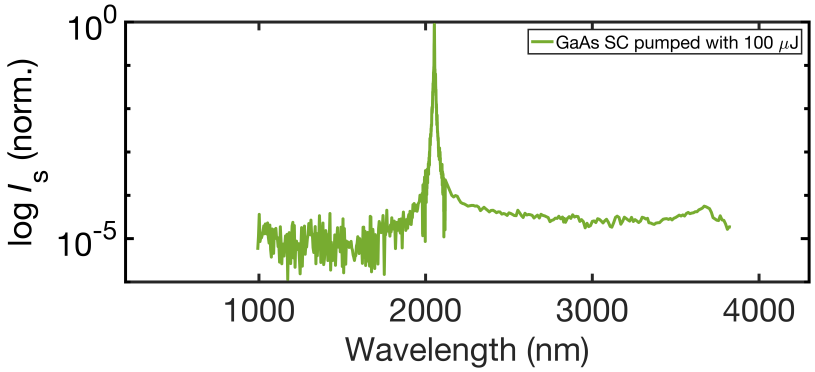


Figure 2.12: Representative SC spectrum from 1 $\mu$m to 4 $\mu$m, generated in a 10cm-long GaAs crystal, pumped with 100 $\mu$J.

Firstly, the overall spectrum spanning from 1 $\mu$m to 4 $\mu$m is shown in Figure 2.12. Most of the energy is transferred into the MIR region between 2.1 $\mu$m and 4 $\mu$m (defined at -40 dB). A limited broadened spectral intensity is detected between 1 $\mu$m and 2 $\mu$m. The second harmonic of the pump near 1 $\mu$m is weak (close to -50 dB), because it is very close to the edge of the transparency window of GaAs (0.9 - 17.3 $\mu$m).

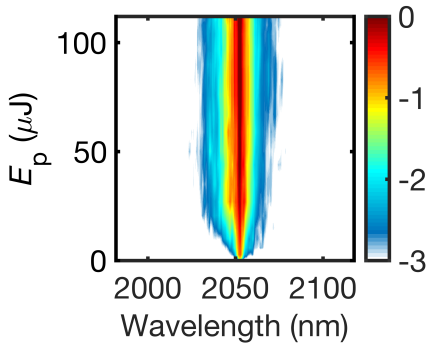


Figure 2.13: Evolution of the normalized SC spectra in logarithmic scale near 2 $\mu$m with respect to pump energy in 10cm-long GaAs crystal.

A closer look at the broadening effect near 2 $\mu$m, as shown in Figure 2.13, reveals that the spectrum is merely extended from 2030 to 2060 nm at -30 dB. In Figure 2.14, the energy is preferentially distributed into the MIR region. We can observe the distinct difference between SC in the NIR and the MIR region. On the red-shifted side, the spectral intensity forms a broad plateau at -40 dB compared to the pump intensity, but the NIR part of the SC is comparable to the noise floor of the spectrometer. As denoted in Tab. 2.1, the energy threshold for SC generation is as low as 0.14 $\mu$J. Therefore, SC starts promptly on pumping, but the GaAs crystal is more vulnerable to the pumping, as the fluence threshold of damage is measured at 0.12 J/cm$^2$ ( 96 $\mu$J with a diameter of 340 $\mu$m).

Figure 2.15 shows the deteriorated far-field spatial profile of the beam with signs of multiple filaments, which is also affected by the strong absorption of the crystal itself and the atmosphere. Only 3% energy of the input, including the 2-$\mu$m pump, is transmitted through the 10cm-long GaAs crystal.

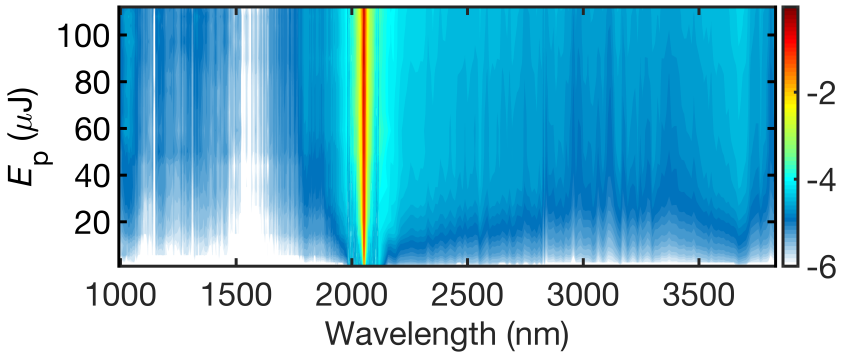


Figure 2.14: Overall evolution of normalized SC spectra in logarithmic scale from 1$\mu$m to 4 $\mu$m as a function of pump energy in a 10cm-long GaAs crystal.

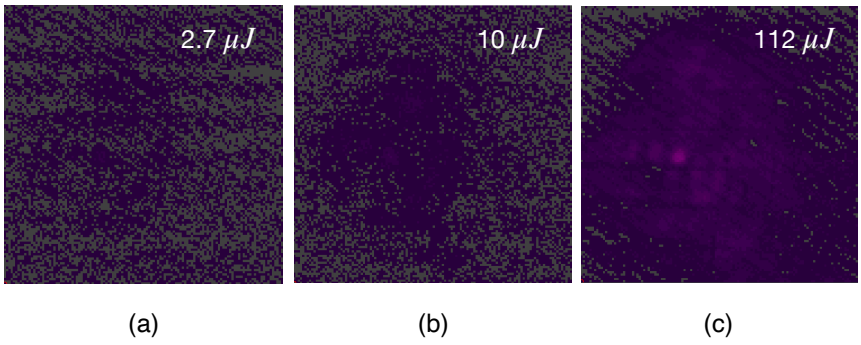


Figure 2.15: Beam profiles in the far field pumped with (a) 2.7 $\mu$J, (b) 10 $\mu$J, (c) 112 $\mu$J after the 10cm-long GaAs crystal.

### 2.4.3 *Discussion*

The interplay between high-order dispersion (which are opposite in the normal and the anomalous dispersion regimes) with non-linearity & plasma effects leads to different temporal dynamics as the pulse propagates in the bulk medium. Consequently, the SC has different spectral profiles in the two cases.

In Figure 2.16, it is clear that the spectral intensity of YAG in the anomalous dispersion regime is at least $\sim$ 10 dB higher than that of the other two crystals over the entire SC range. A significantly spectrally broad third harmonic is observed in YAG. This may be attributed to self compression in the anomalous dispersion regime by the counteraction between the negative dispersion in YAG & the SPM-induced positive dispersion. For the other two semiconductors, the spectral intensity of the central portion of

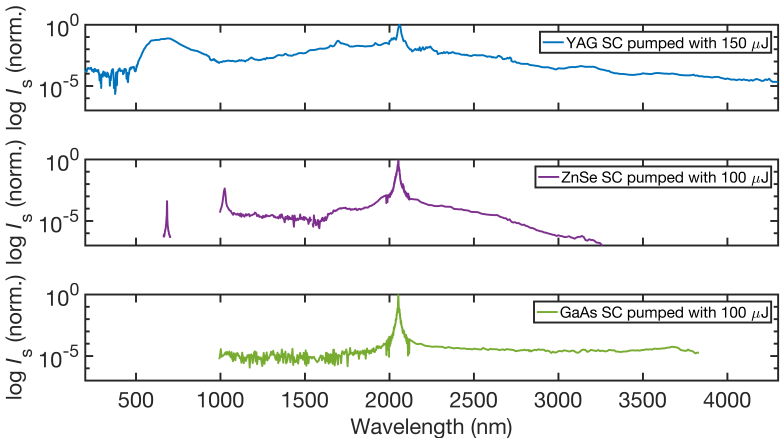


Figure 2.16: Typical overall SC spectra in YAG, ZnSe and GaAs pumped with 150 $\mu$J, 100 $\mu$J & 100 $\mu$J, respectively.

the SC spectrum in ZnSe is stronger compared to that in GaAs, while the SC energy from GaAs is more evenly distributed in the MIR range above 2.5 $\mu$m, compared to ZnSe.

With regard to the evolution of the visible '3$\omega$' in SC with increasing pump energy, in Figure 2.18 (a),(d), and (h), the prominent third harmonic of 2 $\mu$m at 684 nm is obtained both in YAG and ZnSe, but not in GaAs, since the transparency cutoff edge is at 1 $\mu$m. The threshold of THG for the 15cm-long YAG is close to 40 $\mu$J when the SC extends above 2.2 $\mu$m. It is obvious that the third harmonic in ZnSe appears spectrally narrower than that in YAG, partially because it is close to the edge of the transmission window of ZnSe (<50% between 500-600 nm). Another reason might be ascribed to less spectral broadening and insufficient intensity compared to YAG at the central wavelength and inadequate phase matching condition for THG in polycrystalline ZnSe. No SHG is observed in YAG, due to no quadratic nonlinearity in inversion-symmetry.

In Figure 2.18 (b), (e), and (i), SC generation at center wavelength is demonstrated. Enhanced spectral broadening in YAG due to self-compression is observed.

Regarding MIR (beyond 2.5 $\mu$m) components of SC, GaAs possesses more uniform spectra over the entire map. Since there is only 0.14 $\mu$J required for initiation of SF ( $P_{cr}$= 0.045 MW), leading inadvertently to multi-filaments. This can also be examined by the diffraction pattern in Figure 2.17.

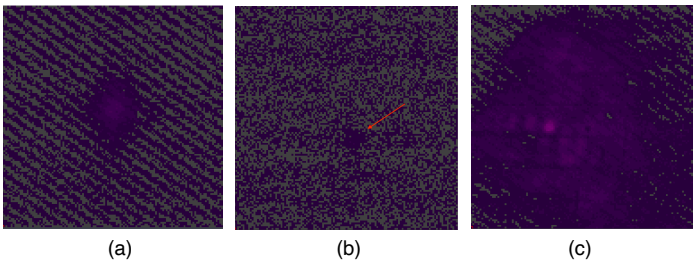


Figure 2.17: Beam profiles after a 2.4 $\mu$m long-pass filter in the far field from (a) a 15cm-long YAG, (b) a 15cm-long ZnSe and (c) a 10cm-long GaAs, pumped with 112$\mu$J with 2-$\mu$m 3-ps pulses.

In YAG and ZnSe, the thresholds of SC are $\sim$ 12 $\mu$J and $\sim$1 $\mu$J, respectively. Distinct spectral broadening in both crystals is witnessed around $4P_{cr}$. The MIR spectrum in YAG extends to $\sim$ 3.2 $\mu$m. Similarly, for ZnSe, it extends to 3 $\mu$m, which is sufficient for seeding OPAs/OPCPAs.

In conclusion, GaAs is less suitable for 2$\mu$m, 3-ps pumped SC generation in terms of spectral intensity and spectral coherence. However, SC in GaAs extends deeply into the MIR region. The drawback is that SC in GaAs needs to be weakly pumped. Otherwise, the spectral density is low and there is a propensity to produce multiple filaments, which will jeopardise the coherence of the SC spectrum. However, the fluctuation of the pump energy and the inclination to trigger MI in the anomalous dispersion regime destabilises the output SC and therefore the output of following OPA/OPCPA stages. SC generation in ZnSe is relatively weak in spectral density in the MIR region, but more stable compared to that in YAG.

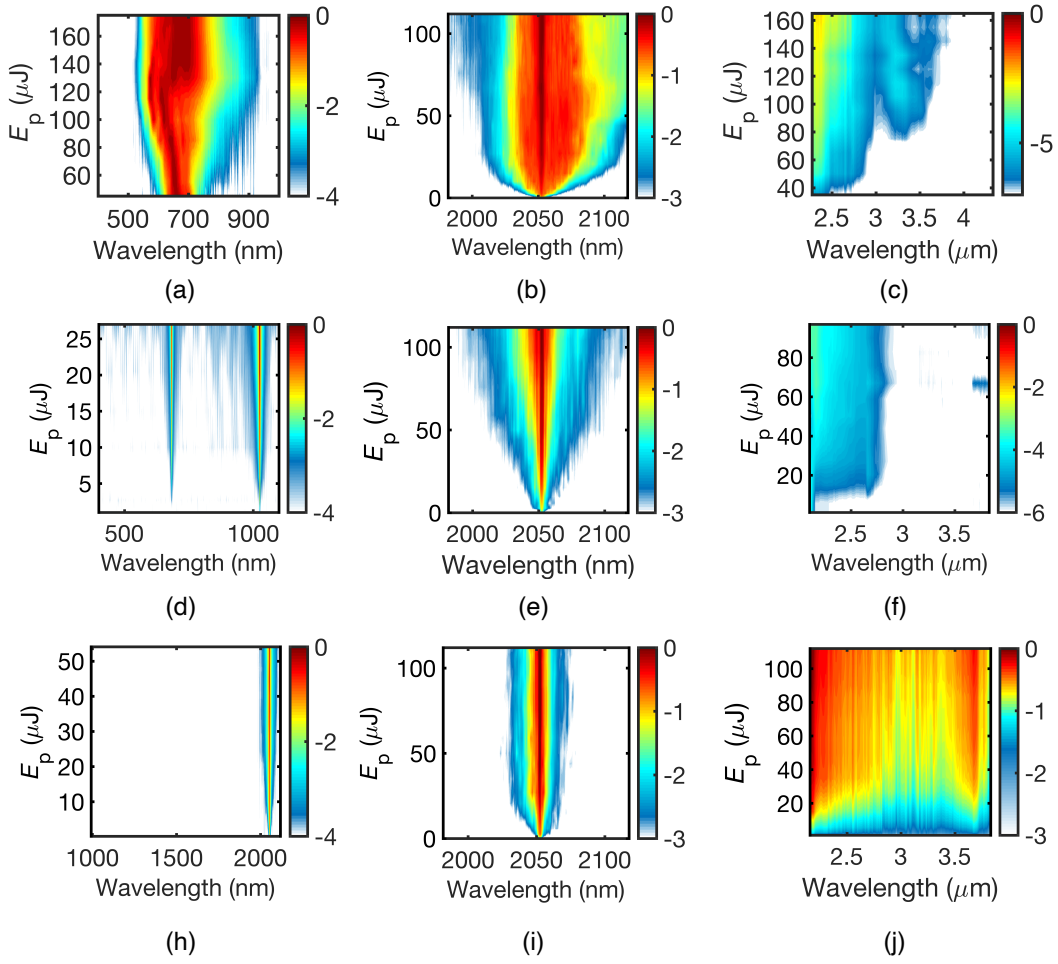


Figure 2.18: SC spectral dynamics in YAG (a, b, c), ZnSe (d, e, f), and GaAs (h, i, j) under different pump energies.

# 3

# DESIGN AND SIMULATION OF OPTICAL PARAMETRIC AMPLIFICATION

## 3.1 PRINCIPLES OF OPA

In the series expansion of polarization in (2.1), the second-order nonlinearity ($\chi^{(2)}$) is responsible for various nonlinear phenomena, such as second-harmonic generation (SHG) and difference-frequency generation (DFG). Its contribution to nonlinear polarization is described in equation (3.1). Different from $\chi^{(3)}$ phenomena involved in SC generation presented in Chapter 2, all second-order nonlinear processes only happen in non-centrosymmetric materials, since $\chi^{(2)}$ would disappear as inversion symmetry is satisfied in centrosymmetric materials, such as in a glass, liquids, gases, etc.

$$\widetilde{P}^{(2)}(t) = \epsilon_0 \chi^{(2)} \widetilde{E}^2(t) \tag{3.1}$$

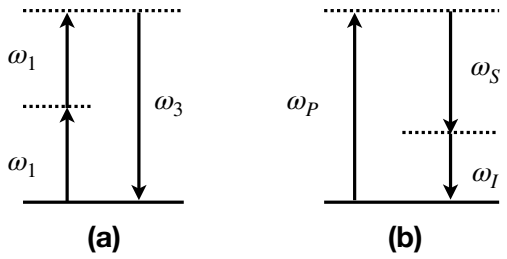


Figure 3.1: (a) second-harmonic generation (SHG); (b) difference-frequency generation (DFG).

Assuming the optical field possesses two different frequencies ($\omega_1$, $\omega_2$) presented below, the electric field may be written as

$$\widetilde{E}(t) = E_1 e^{-i\omega_1 t} + E_2 e^{-i\omega_2 t} + c.c. \tag{3.2}$$

Inserting into equation (3.1), we could derive

$$\begin{aligned}\widetilde{P}^{(2)}(t) = \epsilon_0\chi^{(2)}[{E_1}^2 e^{-i2\omega_1 t} + {E_2}^2 e^{-i2\omega_2 t} + c.c.] \\ + 2\epsilon_0\chi^{(2)}[E_1{E_2}^* e^{-i(\omega_1-\omega_2)t} + c.c.] \\ + 2\epsilon_0\chi^{(2)}[E_1 E_2 e^{-i(\omega_1+\omega_2)t} + c.c.] \\ + 2\epsilon_0\chi^{(2)}[E_1{E_1}^* + 2E_2{E_2}^*]\end{aligned} \tag{3.3}$$

Each line of the right-hand side represents SHG, DFG, sum frequency generation (SFG), and optical rectification (OR), respectively. Intrinsically, OPA is a DFG process, the main difference being the unequal intensities between the pump ($\omega_1$) and the signal ($\omega_2$). Stimulated by the presence of an initial weak signal, the pump with much higher intensity transfers its energy into two frequency components $\omega_2$ and $\omega_3$, so that the signal at $\omega_2$ is amplified and new photons at $\omega_3$, called *the idler*, are generated. Since the signal is amplified, its amplified intensity will enhance the generation of the idler; likewise, the idler will re-boost the generation of the signal. This positive feedback loop enables very high gain for the increase of both the optical fields. All frequencies involved in this exponential amplification satisfies the energy conservation relationship:

$$\hbar\omega_1 = \hbar\omega_2 + \hbar\omega_3 \tag{3.4}$$

Apart from the law of energy conservation, momentum conservation indicated in equation (3.5) has to be satisfied as well, which means that certain phase-matching conditions have to be assured. Thus, it also explains why normally only one parametric process expressed in the right-hand side of equation (3.3) is observed at a given time.

$$\hbar\boldsymbol{k}_1 = \hbar\boldsymbol{k}_2 + \hbar\boldsymbol{k}_3 \tag{3.5}$$

Therefore, practically, to obtain photons at an aimed frequency, an appropriate crystal with carefully designed orientation, as well as the polarizations, frequencies, and directions of the input electric fields have to be taken into consideration.

## 3.2 NONLINEAR CRYSTALS

In order to exploit the capability of OPA/OPCPA technique, the selection of a proper nonlinear crystal for DFG or OPA is the first key step.

| Crystal | Nonlinear coefficient $d_{eff}$(pm/V) | Transmission range ($\mu$m) | Damage threshold ($GW/cm^2$) |
|---|---|---|---|
| BBO | 2.3 ($d_{22}$) | 0.19-3 | 16 (50 ps)[77] |
| KTA | 2.2 (type II)[22] | 1.5-4.5 | 200 [23] |
| AGS | 31 | 0.47-13 | 1-1.5 (50 ps) [78] |
| AGSe | 33.9 [79] | 0.78-18 [80] | > 200 (26 fs)[79] |
| CSP | d14=53, d36=84.5 @4.56um [81] | 1-6.5 | > 4.5 (8 ps) [82] |
| LGS | 5.6 | 0.33-11.6 | 50 (1 ps) [35] |
| GaSe | 35[34] | 0.62-20 | 1700[83] |
| ZGP | 79 [84] | 2.0-8.5 | 10* (3 ps) |

Table 3.1: Comparisons between different OPA crystals, *: experimental result described in this thesis.

The common DFG crystals for the generation of infrared pulses are listed in Tab. 3.1. It is clear that oxide crystals, such as BBO and KTA, are only transparent up to around 3 $\mu$m due to multiphoton absorption, and are therefore not capable of generating MWIR or LWIR (above 4 $\mu$m) through the different-frequency mixing process. In order to enable the generation of wavelengths beyond 4 $\mu$m, researchers resort to other commercially available nonlinear crystals listed in Tab. 3.1, such as AGS, AGSe, GaSe, etc.

In order to bridge the gap between commercially available laser systems at 800 nm or 1 $\mu$m and aimed wavelengths in MWIR/LWIR, the most commonly used approach is to build transitional cascaded OPA/OPCPA stages. Thus, these transitional OPA/OPCPA stages are normally based on KTA or BBO [85, 86].

The other strategy is to begin with a 2 $\mu$m laser source instead of laser sources at 800 nm or 1 $\mu$m. This has recently come to attention to exploit the nonlinear crystal, ZGP, whose transparency window starts from 2 $\mu$m. ZGP possesses multiple advantages over other candidates with high damage threshold (5 J/cm$^2$), high nonlinearity (77-81 pm/V), and availability of large apertures (10 $\times$ 10 mm$^2$).

A hitherto unexplored potential application of ZGP-based OPA schemes is in the area of vibrationally-controlled strong-field chemistry [87]. The unique advantages of ZGP, namely the high-energy OPA output it enables, combined with its high transparency in the 2-8 $\mu$m regime, make it an ideal candidate for facilitating the non-linear vibrational excitation of both high-frequency stretch modes (typically $\lesssim 5$ $\mu$m or $\gtrsim 2000$ cm$^{-1}$) as well as low-frequency bend or torsional modes (typically $\lesssim 2000$ cm$^{-1}$) in most molecules. This provides potentially new routes towards probing uncharted territories in vibrationally-mediated photochemistry [6], coherent control of vibrational dynamics [8], and two-dimensional infrared (2D-IR) spectroscopy [5].

In the laboratory, the experimental requirements warrant a versatile and flexible laser design, with emphasis on the effortless tuning across the molecular fingerprint regime and adjusting the spectral bandwidth for either mode-selective vibrational excitation or concurrent excitation of multiple key vibrational modes for 2D-IR spectroscopy. Compared to high-harmonic generation, the criterion on pulse energy is relaxed to at least the order of a few tens of $\mu$J, since it is dictated by the absorptivity of the targeted vibrational mode(s) for non-linear excitation, taking into account the losses introduced by dynamic pulse-shaping techniques for coherent control – typically, MIR acousto-optic modulator (AOM) as [88]. This has so far not been feasible, owing to the paucity of high-energy OPA schemes for wavelengths exceeding $\sim 5$ $\mu$m.

PHASE MATCHING Figure 3.2 lists different phase-matched signals as the function of incident angle 'alpha' ($\alpha$) between the pump and the signal for 2mm-and 5mm-thick ZGP crystals at three different PMA ($\theta$) of 52°, 54°, and 56°, respectively. We can conclude that (i) as $\theta$ is fixed, thinner crystal benefits phase matching for broader bandwidth; (ii) for different $\theta$ but with same thickness, ZGP designed at 52° owns broadest phase-matching bandwidth while having less tolerance to $\alpha$ (< 1°); (iii) calculated wavelength of the corresponding idler ranges widely from 4 to 10 $\mu$m.

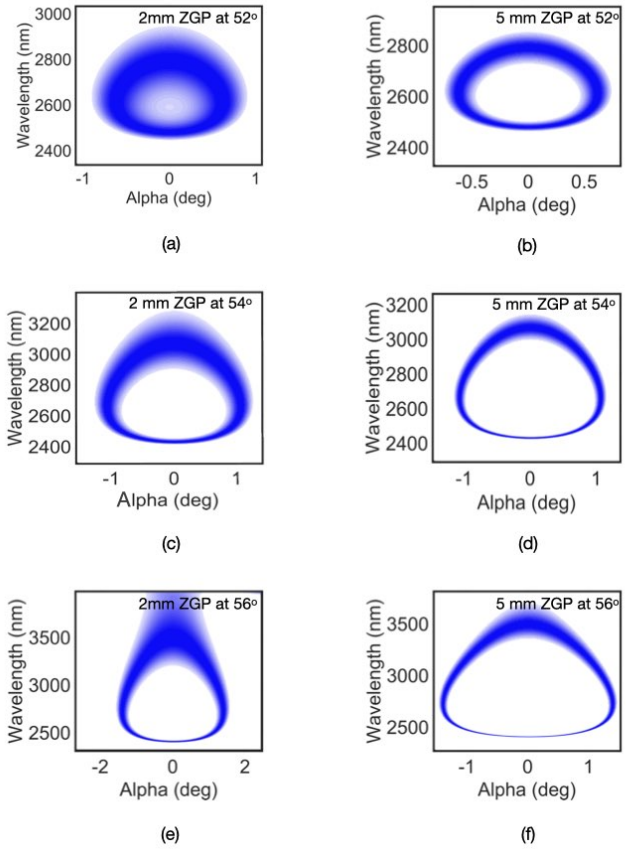


Figure 3.2: Phase matching patterns of 2mm- and 5mm-thick ZGP at 52° (a-b), 54° (c-d) and 56° (e-f), respectively. All data are retrieved from Chi2D [89].

## 3.3 SIMULATION FOR ZGP-BASED OPA WITH CHI2D

While aiming for a high gain during amplification, avoiding back conversion is an important prerequisite for OPA processes. Back conversion is the flow of energy from the amplified signal and the idler back to the pump. It becomes prominent as the length of the crystal increases, which often contradicts with the pursuit of achieving high gain in amplification. Therefore, in order to map out the optimal conditions to obtain high gain but to keep zero or minimal back conversion simultaneously, simulations of the OPA process in ZGP crystals with the help of Chi2D have been conducted in this thesis.

### 3.3.1 *Influence of the crystal length*

In figure 3.3, the blank space to the left in the plots denotes the area where the crystal gets damaged, whereas the blank space to the right is the safe zone, where neither back conversion nor crystal damage happens. Therefore, the colored area is the key region to investigate in order to achieve high gain without the influence of back conversion.

Here we assume the pulse duration of both pump and the seed are 500 fs (FTL), the $1/e^2$ intensity radius of these two beams is identical (i.e. $R_s/R_p = 1$), the energy of the unamplified seed is 10 nJ.

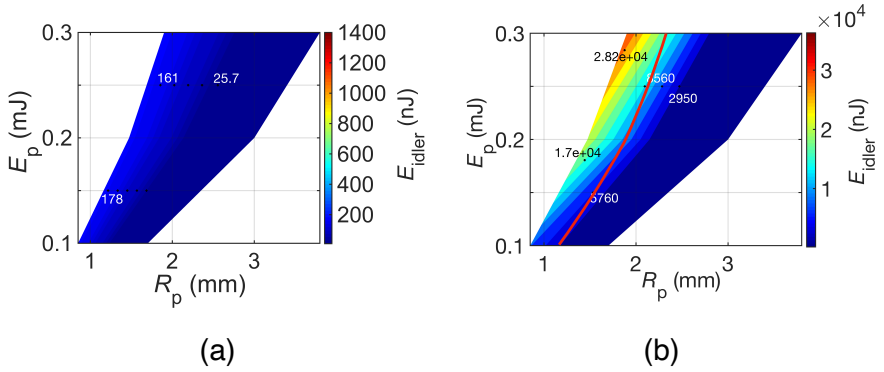


Figure 3.3: Comparison for the energy of the idler from the OPA process as a function of the pump energy $E_p$ and the pump radius $R_p$ in 1-mm thick (a) and 2-mm thick (b) ZGP crystal. The solid red line in (b) indicates the boundary for the initiation of back conversion.

In figure 3.3, no back conversion appears in the 1-mm thick ZGP crystal. However, the maximum energy of the idler without back conversion in the 2-mm thick ZGP crystal is a hundred times higher than the maximum output in the 1-mm thick ZGP crystal. Thus, a 2-mm thick ZGP is preferred because of the high gain and no back conversion. So, in the following simulation, the length of the ZGP crystal is set to 2 mm.

### 3.3.2 *Influence of the spatial overlap*

To simulate the influence of the spatial overlap, the pump duration is set to that of the regenerative amplifier (3 ps) but the pulse duration of the seed is kept to be 0.5 ps. The ratio of the radius between the signal and the pump (i.e. $R_s/R_p$) is selected to be 1, 0.75, 0.5, 0.25. The simulation is shown in figure 3.4. As $R_s/R_p$ shrinks, the maximum energy of the idler increases correspondingly as the gain of amplification is enhanced with the intensity of the seed. However, back conversion is also strengthened along with decreasing $R_s/R_p$.

Because of the back conversion constraint, the globally optimal range of $R_s/R_p$ to obtain the highest energies without back conversion falls between 0.5 and 0.75. As in figure 3.4 (b), the highest energy is $\sim 5.2\ \mu$J when $R_s/R_p = 0.75$.

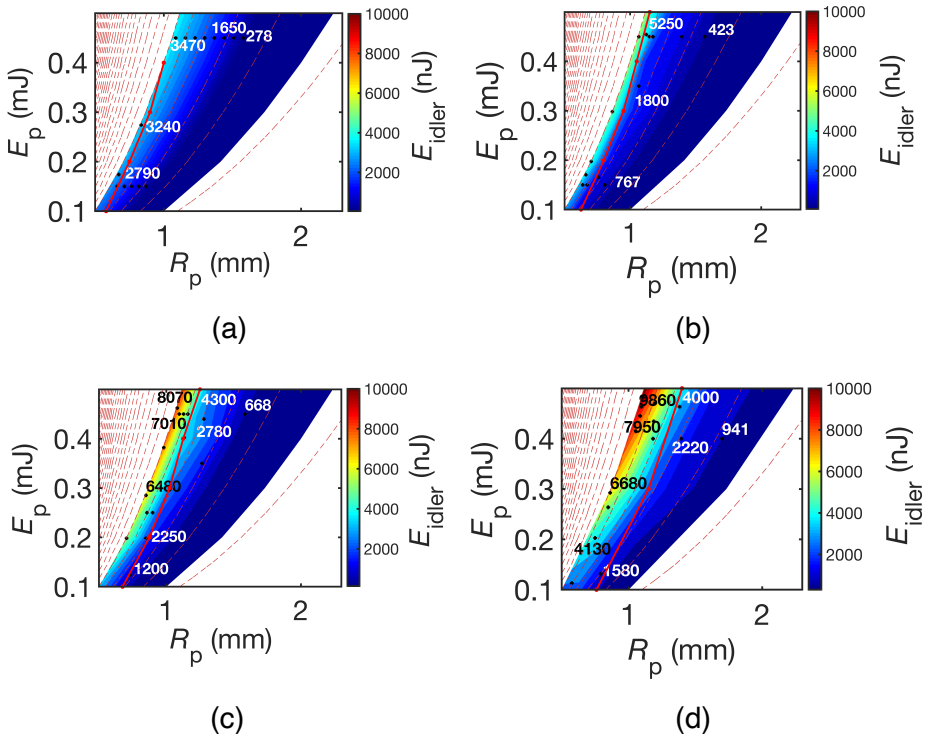


Figure 3.4: Comparison of the energy of the idler from the OPA process as functions of the pump energy $E_p$ and the pump radius $R_p$ in a 2-mm thick ZGP crystal with different spatial overlap $R_s/R_p = 1, 0.75, 0.5, 0.25$ (a)-(d). The solid red line in (b) indicates the boundary of the initiation of back conversion. Along the dash red lines, the pump intensity is identical.

### 3.3.3 *Influence of the temporal overlap*

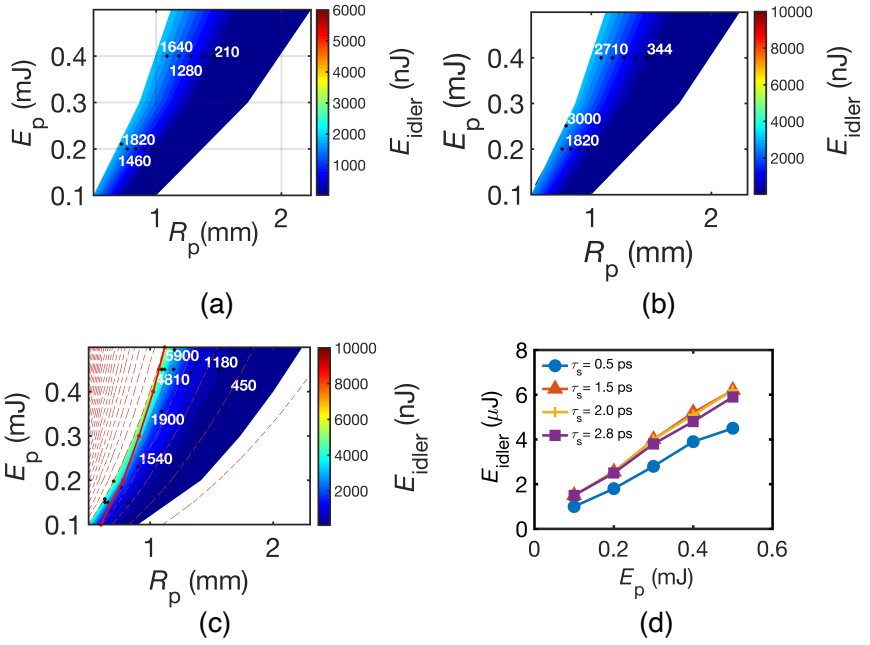


Figure 3.5: Comparison of the energy of the idler from the OPA process as functions of the pump energy $E_p$ and the pump radius $R_p$ in a 2-mm thick ZGP crystal with $R_s/R_p = 1, 0.75, 0.5$ (a)-(c). In (d), the energy scaling of the idler $E_{idler}$ as a function of the pump energy $E_p$ is shown when the seed (FTL: 500 fs) is chirped to different pulse durations.

The influence of the temporal overlap is also investigated. Firstly, we chirp the pulse duration of the signal from 0.5 ps (FTL) to 2.82 ps ($\tau_s/\tau_p = 1$), so that we can compare the energies of the idler with different spatial overlaps. The results are illustrated in figure 3.5 (a)-(c). The comparison reveals that the optimum spatial overlap for $\tau_s/\tau_p = 1$ becomes 0.5. So in figure 3.5 (d), $R_s/R_p$ is set to 0.5. Energy scaling functions of the idler seeded with different chirped pulses at different pump energies are demonstrated in figure 3.5 (d). It suggests that the optimal temporal overlap ($\tau_s/\tau_p$) for avoiding back conversion varies within 0.5-0.67.

### 3.3.4 *Conclusions*

From all the simulations above, we can derive a preliminary guideline for the design of the first-stage OPA:

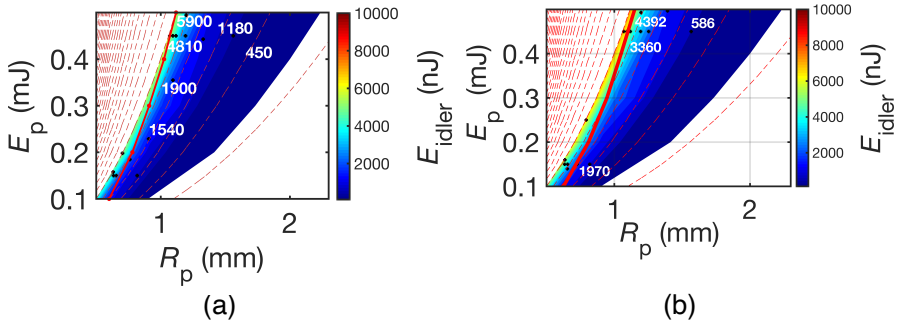


Figure 3.6: Comparison of the energy of the idler from the OPA process as functions of the pump energy $E_p$ and the pump radius $R_p$ in a 2-mm thick ZGP crystal with different seed energies but the same seed intensity; that is, $E_{seed}$= 10 nJ, $R_s/R_p = 0.5$ in (a) and $E_{seed}$= 40 nJ, $R_s/R_p = 1$ in (b).

A. A 2-mm thick ZGP crystal is preferred compared to a 1-mm thick ZGP crystal at the first stage to obtain high gain for seed amplification and suppression of back conversion. Although a 5-mm thick ZGP crystal can provide higher gain for the amplification, we have to increase the diameter of the pump and the seed (> 2.5 mm) so that back conversion can be avoided, when pumped at a high-energy level, which is beyond the clear aperture of the ZGP crystal we have.

B. The influence of the intensities of the pump and seed is investigated through two parameters – spatial and temporal overlap. An optimum spatial and temporal ratio to achieve high gain in amplification without back conversion is between 0.5 and 0.75.

C. Higher energy of the seed can avoid damaging the crystal while maintaining the same energy of the idler.

# 4

# ULTRAFAST OPA TUNABLE IN THE MOLECULAR FINGERPRINT REGIME

## 4.1 YAG-BASED SC-SEEDED ZGP OPA / NOPA

In this chapter, details of YAG-based SC-seeded ZGP parametric amplification under collinear and non-collinear schemes with different PMA, $\theta$, are presented. First of all, collinear and non-collinear schemes for optical parametric amplification and their advantages and disadvantages are briefly introduced here.

*Collinear scheme* means that the pump and the signal or the idler propagate in the same direction. They overlap with each other spatially and temporally in the nonlinear crystal.

A. Wavelength tuning can be easily realized by delaying one beam with respective to the other so that the pump may be overlapped selectively with part of the dispersed signal.

B. Compressibility of the output is easier than the non-collinear scheme because it owns less angular dispersion over a large spectral range.

C. It enables us to tune the wavelength of the signal or the idler easily in a certain range but at the cost of gain and phase-matching bandwidth, compared to the non-collinear scheme.

*Non-collinear scheme*, which denotes that the pump and the signal are incident at an angle $\alpha$, is usually preferred owing to the following merits:

A. Wavelength tunability is over a large range. For example, the idler can vary over a spectral range of a few microns. As shown in figure 3.2 (c), the idler in ZGP at $\theta$=54° is able to vary from 5 to 7 $\mu$m.

B. Broader phase-matching bandwidth may support a few-cycle pulse. As indicated in figure 3.2 (a), as $\alpha$ deviates from 0° (collinear scheme), the phase-matching bandwidth (~300 nm, foot-to-foot) is nearly two-fold compared to that in the collinear scheme, with an FTL duration of 2-5 optical cycles.

Nonetheless, the output of the non-collinear scheme has a larger angular dispersion. Thus, pulse compression requires more precise dispersion control.

### 4.1.1 *Collinear scheme*

In the collinear scheme, the performance of a single OPA stage with different thicknesses and various PMA for ZGP crystals are investigated.

Figure 4.1 demonstrates the performance of a single OPA stage with a 2 mm-thick ZGP at different PMA. A 2-mm thick ZGP at 52° has broader phase-matching bandwidth and is preferrable for amplification at a longer wavelength, as indicated in figure 4.1, which is consistent with theoretical simulations shown in figure 3.2.

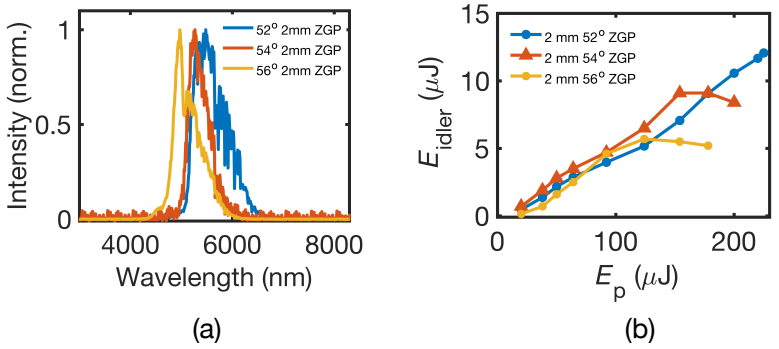


Figure 4.1: Representative performance of the idler from a single OPA stage based on a 2-mm thick coated ZGP crystal on seeding with SC from YAG. The wavelength of the idler at different PMA, $\theta$ (a); energy scaling as a function of the pump energy $E_p$ of 3-ps 2-$\mu$m source (b).

For a 5 mm-ZGP OPA, we only compare the two different values of $\theta$, 52° and 54°, since a 5-mm, 56° ZGP-based OPA is inclined to

generate the signal and the idler at the degenerate point, which deteriorates the behaviours with respect to the amplification and the spectral profile. Here, identical central wavelengths of the idlers in a 5-mm thick ZGP at 52° and 54° are demonstrated in figure 4.2. Figure 4.3 reveals that ZGP at 52° is superior to ZGP at 54° at 5 $\mu$m in terms of energy scaling.

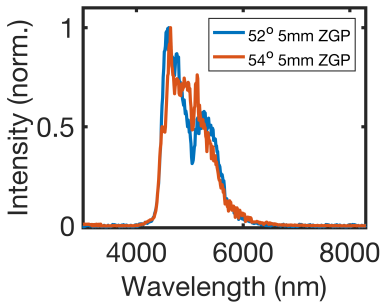


Figure 4.2: Idler spectra from 52° and 54° 5-mm thick ZGP OPAs.

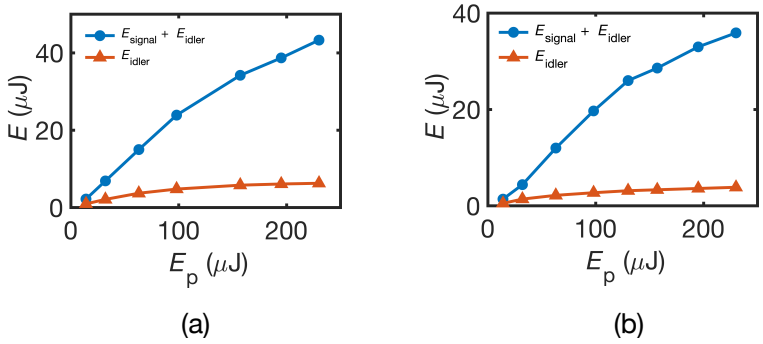


Figure 4.3: Energy scaling function of the signal and the idler as versus pump energy $E_p$ from OPA based on 5mm-thick 52° ZGP (a) and 54° ZGP (b).

### 4.1.2 *Non-collinear scheme*

A non-collinear OPA is often called a NOPA. It takes the advantage of the dependence of the phase-matching spectral bandwidth on $\alpha$. Likewise, here in figure 4.6, we firstly compare the idler for ZGP with different thicknesses and PMA in the non-collinear scheme with the same temporal overlap conditions – that is, by fixing the position of the delay stage and the angle $\alpha$, but replacing with different ZGP crystals.

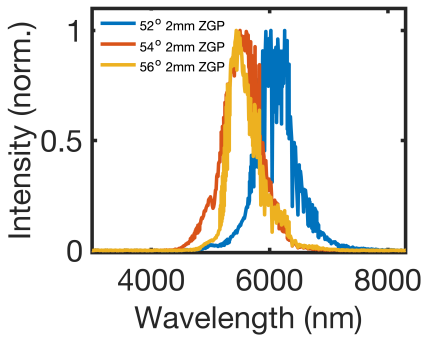


Figure 4.4: Spectra of the idler from the NOPA based on a 2-mm thick ZGP at $52^o$, $54^o$ and $56^o$.

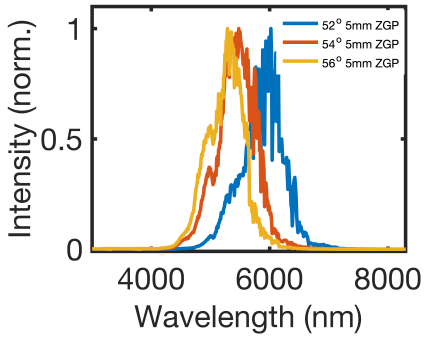


Figure 4.5: Spectra of the idler from the NOPA based on a 5-mm thick ZGP at $52^o$, $54^o$ and $56^o$.

Based on the comparison in figure 4.6, the spectra of the idler from the 2-mm thick ZGP crystals are more symmetric than that of the 5-mm thick ZGP crystals, which results from the group velocity mismatch in the longer crystal. Similarly, 52° ZGP is suitable for phase matching at longer wavelengths. The energy scaling with different parameters is demonstrated in figures 4.7 and 4.8.

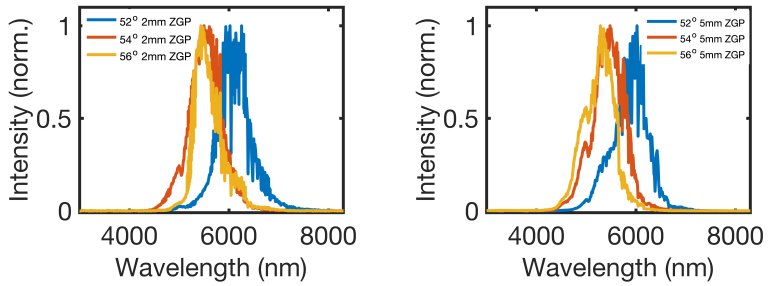


(a) (b)

Figure 4.6: Spectra of the idler from NOPA scheme based on 2mm- thick ZGP (a) and 5mm-thick ZGP (b) at different cutting angle 52°, 54° and 56°.

From figures 4.7 and 4.8, we can notice that a longer crystal length benefits the output energy for 52° ZGP at 6 $\mu$m, but it gradually degrades as the PMA, $\theta$, increases.

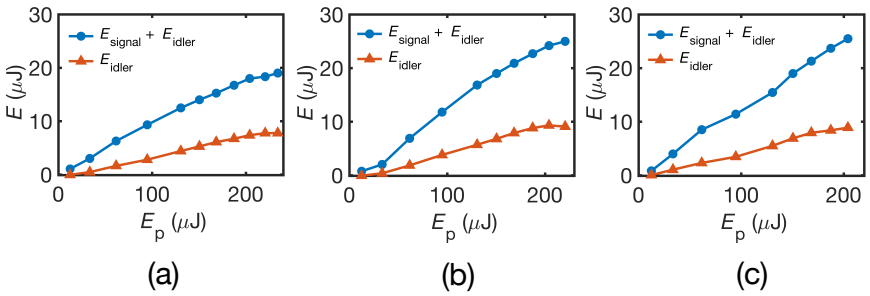


Figure 4.7: Energy scaling of the signal and the idler versus pump energy $E_p$ in the non-collinear scheme based on a 2-mm thick 52° ZGP (a), 54° ZGP (b), and 56° ZGP (c) crystal.

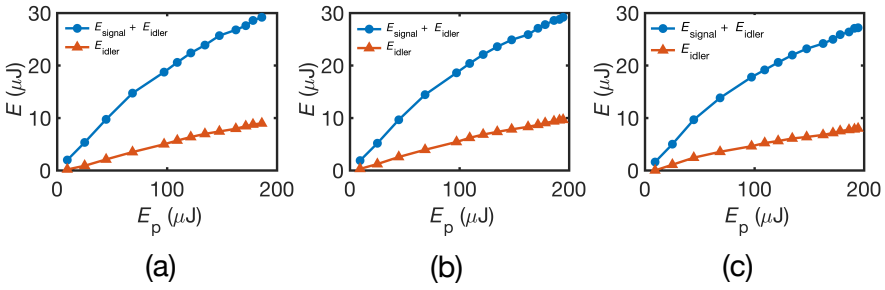


Figure 4.8: Energy scaling of the signal and the idler versus pump energy $E_p$ in the non-collinear scheme based on a 5-mm thick 52° ZGP (a), 54° ZGP (b), and 56° ZGP (c) crystal.

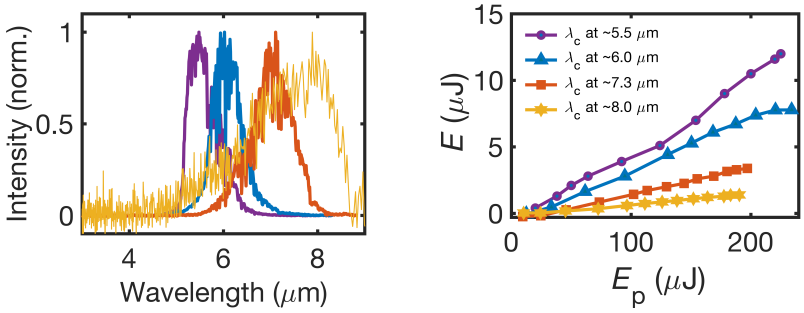


Figure 4.9: Tunable spectra of the idler from the NOPA based on a 2-mm thick ZGP at 52° (a) and its corresponding energy scaling versus the pump energy $E_p$. The idler centred at 8 $\mu$m is measured by a commercial (ArcOptics) ® Fourier-transform infrared spectrometer.

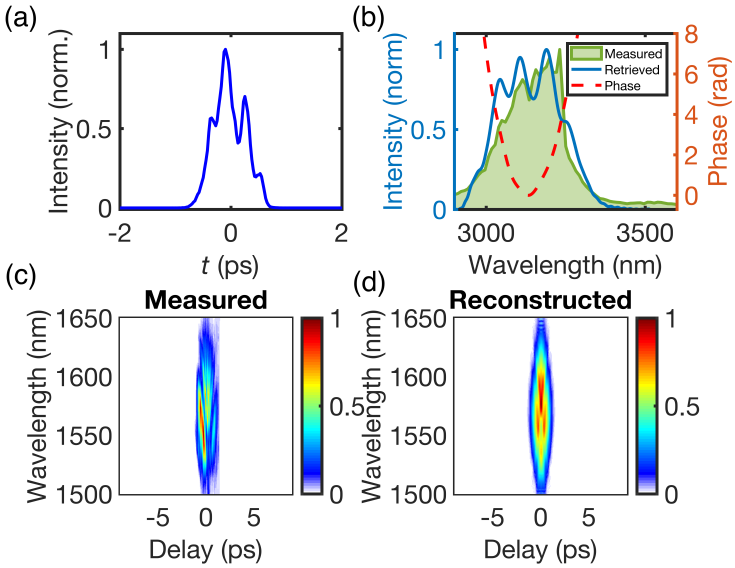


Figure 4.10: Pulse characterization of the signal from a 2-mm thick 52° ZGP in the NOPA scheme, measured by SHG-FROG. The pulse duration is ~0.6 ps (FWHM), where the spectral bandwidth of the signal can support 42 fs (FTL).

The *wavelength tunability*, from a single NOPA stage for a 2-mm thick 52° ZGP crystal, is characterized. Its representative tunable wavelengths (5.5 -8 $\mu$m) and their energy scaling performance are illustrated in figure 4.9. The conversion efficiency is lower at longer wavelengths, due to less interactive length at non-zero $\alpha$ for longer wavelengths.

The *temporal profile* is captured with SHG-FROG. In the previous section, the performance of a single ZGP OPA stage in the spectral domain is described. As mentioned in Chapter 2, YAG-based SC generation has a stability issue and pulse-splitting effects, which would imprint on the output of the OPA process. In figure 4.10, the pulse profile is divided into multiple peaks, which would introduce difficulties during pulse compression. Although the YAG-based SC-seeded single OPA/NOPA stage shows great potential in terms of energy scaling and tunability over a wide spectral range, the aforementioned difficulties divert our strategy into using a ZnSe-based SC-seeded ZGP OPA/NOPA.

## 4.2 ZNSE-BASED SC-SEEDED ZGP OPAS/NOPAS

In this section, we present our ZnSe-based SC-seeded OPAs or NOPAs. In order to be able to tune the spectral output in the range 3-8 $\mu$m, we developed a compact MIR laser architecture, comprising a pair of parallel chains of cascaded ZGP-based OPA/NOPAs as depicted in figure 4.11. This allows ready tunability in the molecular fingerprint regime and is tailored for strong-field excitation and coherent control of both stretch and bend (or torsional) vibrational modes in molecules. Furthermore, it can afford a higher energy yield ($\lesssim 60$ $\mu$J at 1 kHz) compared to most conventional OPA gain media transparent in the $2-8$ $\mu$m wavelength range.

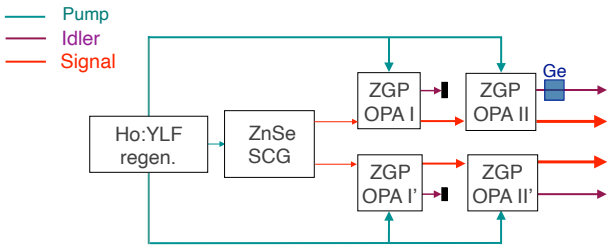


Figure 4.11: Schematic of the experimental setup [90]. A Ho-doped fiber oscillator (shown in Appendix A) seeds a Ho:YLF RA [37], which is used to pump SC generation in ZnSe [67] and chains of ZGP OPAs in parallel. A representative scenario of the idler compression by dispersion compensation in Ge is also shown.

The compressibility of the output is also demonstrated here by a representative measurement of the near-Gaussian temporal profile of a dispersion-compensated 105-fs idler pulse at a central wavelength of 5.1 $\mu$m, corresponding to $\sim$ 6 optical cycles. Detailed numerical simulations closely corroborate the experimental measurements, providing a benchmark and a platform to further explore the parameter space for future design, optimization and implementation of high-energy, ultrafast, mid-infrared laser schemes.

The first demonstration of a ZGP-based OPCPA was by Sanchez *et al.* [28], who reported a chain of ZGP OPAs, seeded by the DFG from a multi-arm fiber-based frequency comb and pumped by a

cryogenically cooled Ho:YLF regenerative amplifier, producing 200 $\mu$J (recently upgraded to 700 $\mu$J [29]) of compressed ($\sim$ 180 fs) pulses centered at 7 $\mu$m at a repetition rate of 100 Hz. A similar OPCPA scheme was subsequently reported by Grafenstein et al. [41], generating 650-$\mu$J (recently upgraded to 1.2 mJ [39]) of near-transform-limited $\sim$ 75-fs pulses, centered at 5 $\mu$m, at 1 kHz. An alternative scheme was reported by Kanai et al. [25], comprising a chain of KTA OPAs, pumped by the second harmonic of a carrier-envelope-phase-stabilized Ho:YAG regenerative amplifier, followed by a final ZGP-based OPCPA, generating 40 $\mu$J of 100-fs pulses centered at 5.2 $\mu$m. Although undeniably impressive, these complex laser architectures, aimed at high energy extraction at a given mid-infrared wavelength are not easily amenable to routine, adaptable spectral tuning.

### 4.2.1 *Setup scheme*

Different from the schemes mentioned above, assisted by SC generation, we can construct a compact system as shown in figure 4.11. It relies on the linearly chirped broadband MIR SC, allowing easy tunability, interchangeable between a near-collinear and a non-collinear geometry. Although output energies of the order of $\sim$ 60 $\mu$J (signal and idler combined) at 1 kHz can easily be achieved, the resulting pulse is marred by high-order dispersion effects and accumulation of non-linear phase contributions, impairing pulse-compression schemes and creating convoluted temporal profiles, consistent with previous observations for ZGP OPCPAs [25, 41].

Figure 4.12 shows one arm of the parallel-chain NOPA system. The output of our Ho:YLF regenerative amplifier comprises near-transform-limited, 3-ps pulses at a wavelength of 2052 nm and with a spectral bandwidth of $\sim$ 2 nm [37]. One arm of the output, with 10-20 $\mu$J energy, is focused into a 15-cm long ZnSe crystal, with a numerical aperture as low as $\sim$0.005, in order to circumvent avalanche-ionization-induced breakdown [67]. The SC generated, after collimation, is successively transmitted, first through a MIR beam splitter ( 50%: 50% split ratio) to separate the spectral components relevant for seeding (as shown in Fig. 4.15),

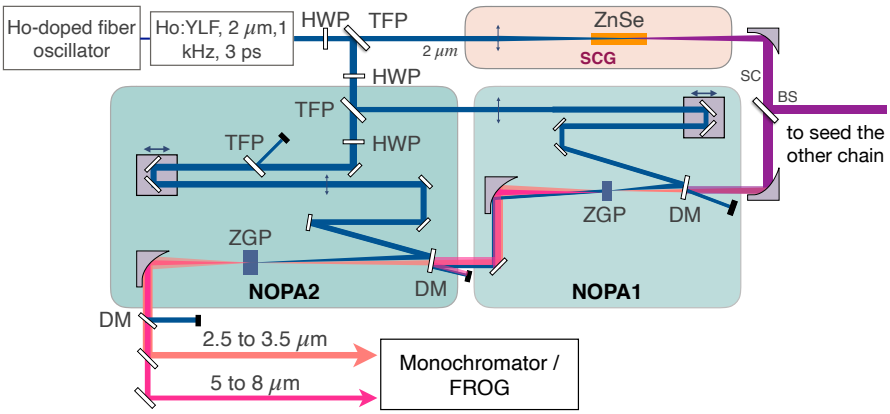


Figure 4.12: Representative details of a one-chain NOPA setup. HWP: half-wave plate; TFP: thin film plate; DM: dichroic mirror; SCG: SC generation; BS: beam splitter.

and then through a custom-made, suitably anti-reflection-coated dichroic mirror (DM) (Layertec), optimized for high reflection efficiency at the pump wavelength. Another arm of the regenerative amplifier output (with variable energy), serving as the pump for the first OPA stage, is appropriately time-delayed and recombined at an adjustable angle with the SC seed after reflecting off the DM.

Both the pump and the seed can be independently and variably focused, and changing their relative time-delays while observing the idler estimates the cross-correlation time as 6.4 ps (foot-to-foot). This is representative of the temporal overlap between the pump ($\sim$ 3 ps) and the corresponding phase-matched spectral bandwidth in the chirped SC seed.

The seed is intentionally not stretched to overlap the entire phase-matched seed spectrum with the peak of the pump pulse, leading to a broad amplified bandwidth and therefore a short pulse duration, while compromising on conversion efficiency [91]. Additionally, this facilitates reduced pulse-to-pulse fluctuations arising due to the timing jitter between the pump and the seed. The first OPA stage consists of a 2-mm thick anti-reflection-coated ZGP crystal ($\theta = 54^\circ$, BAE Systems) with a measured damage threshold of $\sim 5\,\mathrm{J/cm^2}$.

### 4.2.2 *The capability of MIR amplification*

The amplified signal from the first OPA stage, ~ 1 $\mu$J in energy for a pump energy of 100 $\mu$J, has a pulsewidth of 420 fs (FWHM), measured with SHG-FROG. It is propagated to the second OPA stage, consisting of a 5-mm thick ZGP crystal, but otherwise identical to the first OPA stage. The output from the second OPA stage is demonstrated in figure 4.13, generating up to $50-60$ $\mu$J of combined signal and idler energy at 1 kHz for idler wavelengths in the range $5-7$ $\mu$m for pump energies of $250-400$ $\mu$J.

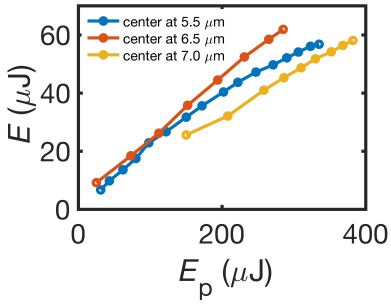


Figure 4.13: Energy scaling of combined signal and idler versus pump energy $E_p$, for three different idlers centred at 5.5 $\mu$m, 6.5 $\mu$m, and 7.0 $\mu$m.

However, careful optimization is required, particularly at high pump intensities to suppress superfluorescence, which competes with the weakly seeded output since the SC seed is shared between the two OPA chains. Moreover, increasing the SC pump energy introduces nonlinear distortions of the seed spectral and temporal phase, the striking deteriorations of which are revealed in SHG-FROG measurements. The entire setup is purged with dry air to minimize atmospheric water-vapor absorption at MIR wavelengths.

As the RA produces higher energy at lower repetition rates and lower temperatures, further energy scaling in the MIR by adding further ZGP stages is possible.

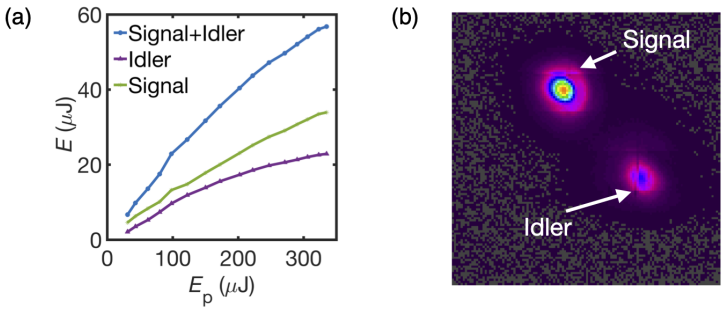


Figure 4.14: (a) The energy scalability of one arm of the system at 5.5 $\mu$m is presented. Combined signal and idler are amplified to $\sim$ 60 $\mu$J for a pump energy of 330 $\mu$J; (b) beam profiles of the amplified signal and the amplified idler in the far field captured by a MIR camera.

### 4.2.3 *The tunability in the fingerprint regime*

Apart from the great potential of high-energy performance in MIR, easy access, and tunability in the fingerprint regime (3-8 $\mu$m) is demonstrated.

The chirped broadband SC in the 15-cm long ZnSe crystal facilitates an effortless tuning of the orientation of the ZGP crystals, along with the angle of incidence and the relative time delay between the pump and the seed.

Figure 4.15 depicts the spectral tunability of the OPAs, measured using a MIR spectrograph with a liquid-nitrogen-cooled MCT array detector, the sensitivity of which declines sharply beyond 8 $\mu$m. Together, the signal and the idler may therefore be flexibly adjusted in order to access both stretch and bend or torsional molecular vibrational modes within the transparency window of ZGP.

Moreover, tunability beyond 8 $\mu$m up to 12 $\mu$m is possible, although with reduced efficiency.

### 4.2.4 *The compressibility with bulk medium*

The compressibility of the output is difficult, as not only does it depend on the intensities of the pump and the signal, but also on their nonlinear dispersion, which is also affected by their intensities.

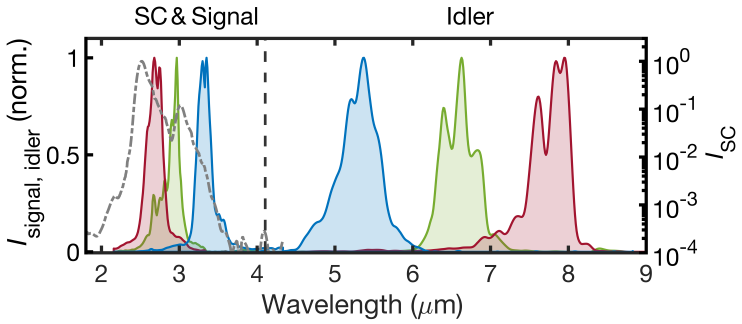


Figure 4.15: The self-normalized spectral intensity of the signal and the corresponding idler (shaded colored plots) on a linear scale on tuning the output wavelengths of the two-stage ZGP OPA for a non-collinear geometry. The sharp cut-off at 8 $\mu$m is due to the drastic decrease in the sensitivity of the MCT detector used as well as the decrease in the transparency of ZGP. The SC seed, generated in a 15-cm long ZnSe crystal pumped at 20 $\mu$J and measured after a 2.4-$\mu$m longpass filter, is also depicted (black dotted line) on a logarithmic scale. The central dotted vertical line represents the degenerate wavelength [90].

#### 4.2.4.1 *Difficulty in compression*

To visualize the dynamical variation of the pulses under different conditions, a series of simulations from Chi2D [89] and typical FROG measurements in the lab are presented.

In order to simulate the OPA process for the second stage, we consider the 1-$\mu$J chirped SC at 3.39 $\mu$m from the 1st OPA stage as the seed for the 2nd OPA stage, pumped with 3-ps unchirped pulses at 2 $\mu$m. As in figure 4.16, the temporal shape of the uncompressed idler is convoluted for pump energies lower than 120 $\mu$J. The difficulty in pumping at lower energies is due to the large GDD and accumulated huge third-order dispersion (TOD) ( $10^6$ $fs^2$) originating from the OPA process and the humidity in the air, which is hard to compensate simultaneously merely with a bulk medium. This is also the reason why Bock et al. resorted to implementing a spatial light modulator (SLM) to minimize the overall TOD of the whole system at the initial stages [39].

#### 4.2.4.2 *Experimental results*

In order to characterize the signal and the idler pulses, an SHG-FROG is assembled, using a 2-mm thick GaSe crystal and coupled to the mid-infrared spectrograph. An example of a typical SHG-FROG measurement is depicted in Fig. 4.17. The group delay dispersion compensation required for pulse compression is estimated from an initial SHG-FROG measurement of the uncompressed idler (shown in Fig. 4.17a, along with the Fourier-transform-limited pulse profile). The introduction of an anti-reflection-coated 30-mm thick Ge window results in a compressed pulsewidth of 105 fs (also shown in Fig. 4.17a) with the added advantage of introducing virtually no energy loss during compression. The measured FROG profile of the compressed idler is shown in Fig. 4.17c, where the retrieval (Fig. 4.17d) corresponds to the optimal spectral reconstruction (Fig. 4.17b) and may arguably overestimate the measured pulsewidth. This demonstrates the compressibility of the output of the two-stage OPA, feasible only for moderate pump energies (up to $\sim 350\ \mu$J). The beam profiles without and with Ge window are also demonstrated in figure 4.19 (a) and (b).

The input specifications are dictated by the laser and crystal specifications, aided by our experimental characterization of the incident pump and seed pulses, and the simulation output for the idler is compared to the measured idler features. Figure 4.18 shows an illustrative example, firstly investigating the uncompressed idler energy from the second-stage OPA as a function of the pump energy ($E_p$). It is observed that in the range $E_p = 200 - 350\ \mu$J (corresponding to a pump fluence in the range $1.2 - 2.1\ \mathrm{J/cm^2}$), the idler is compressible to near-Gaussian profiles, both according to simulations as well as verified by a series of SHG-FROG measurements of the idler both before and after compression. For instance, for the representative SHG-FROG measurement shown in Fig. 4.17, the consistency between the experimental measurements and the simulations is compared in the spectral domain (Fig. 4.18b) as well as the temporal domain, both for the uncompressed (Fig. 4.18c) and the compressed (Fig. 4.18d) idler. The corresponding simulated spatio-temporal evolution of the uncompressed and compressed idler pulse is shown

in Fig. 4.18e and Fig. 4.18 f, respectively. For $E_p > 350$ $\mu$J, severe back-conversion effects or cascaded $\chi^{(2)}$ processes are manifested, which may induce higher-order dispersion, particularly for long crystal lengths, thereby rendering compression schemes ineffective, as observed previously [25]. The close correlation between the experiments and the simulations furnishes a benchmark that may be utilized for further optimization of the alignment geometry to increase the idler energy without being susceptible to such detrimental effects.

In summary, we demonstrate a compact ZGP-based MIR laser architecture, where the emphasis is on the easy tunability in the 2-8 $\mu$m spectral range while supporting a significantly higher mid-infrared energy output compared to most conventional OPA gain media in this wavelength regime. Furthermore, the OPA scheme is energy-scalable, depending on the availability of pump energy and large-aperture ZGP crystals for successive OPA/OPCPA stages. The generic recipe outlined here broadens the horizons in terms of the diverse potential applications that ZGP-based mid-infrared sources are amenable to, particularly with a judicious choice of laser and crystal parameters recommended by the simulation tool described here. This may be envisaged to have a pivotal influence in exploring non-linear vibrational couplings in ultrafast molecular dynamics that have so far been restricted by the available energy of the MIR driver at the required wavelengths.

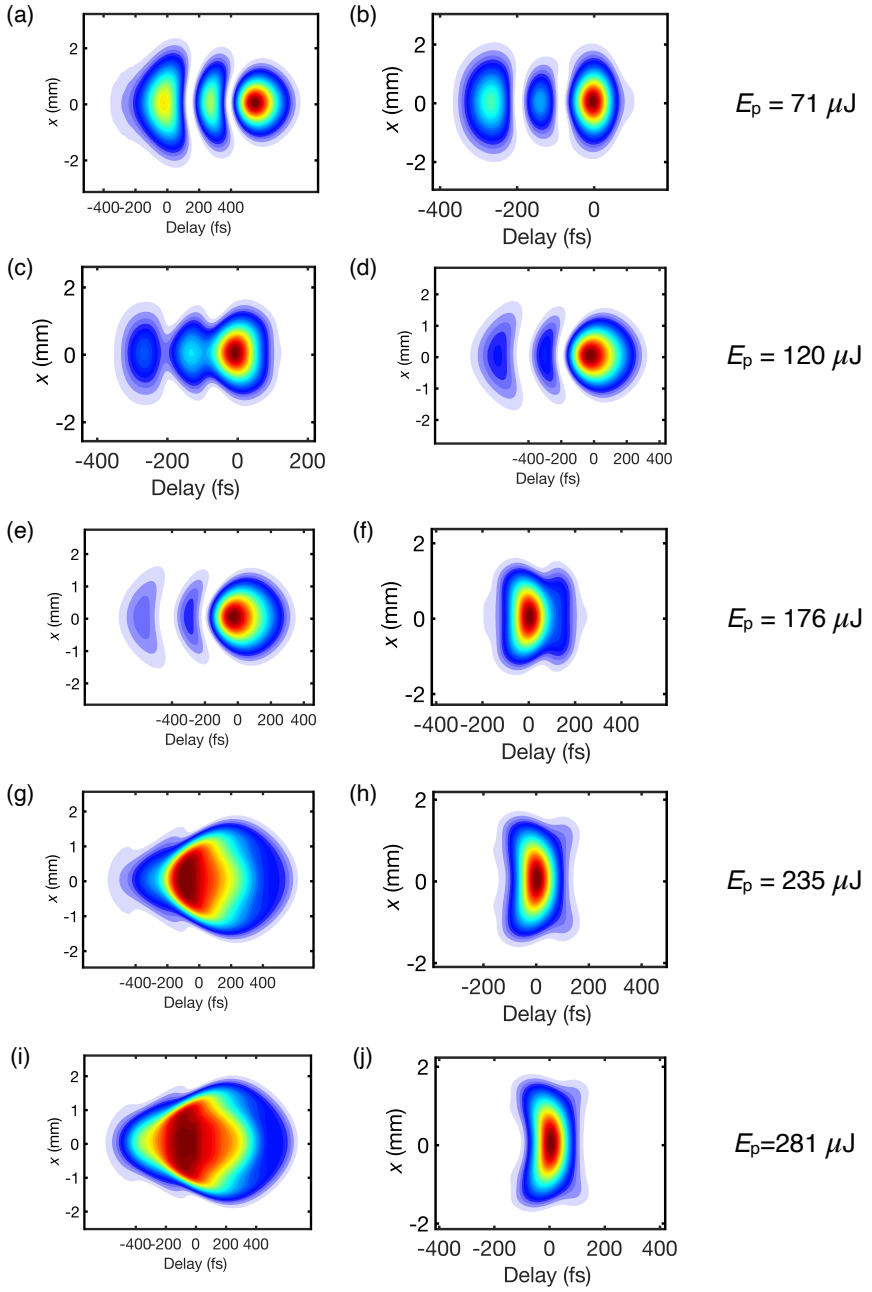


Figure 4.16: Uncompressed (left column) and optimal compressed (right column) temporal and spatial profiles of the idler from the OPA simulated for different pump intensities ($E_p$ = 70 - 280 $\mu$J, $1/e^2$ radius $R$ = 2.5 mm ), on seeding with 1 $\mu$J chirped (GDD = 12000 fs$^2$) SC at 3.39 $\mu$m.

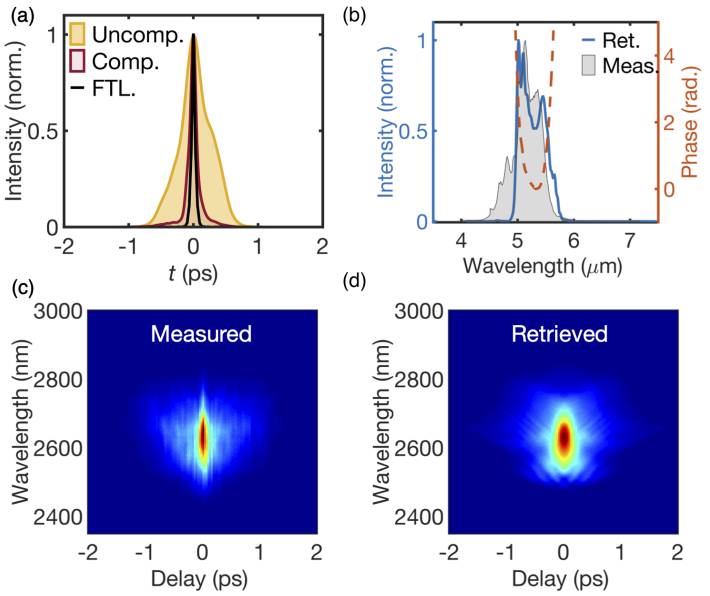


Figure 4.17: Representative SHG-FROG measurement of the compressed idler after transmission through a 30-mm thick Ge window. (a) Retrieved temporal profile of the compressed idler (red) along with the Fourier-transform-limit (FTL, black) with pulsewidths (FWHM) of 105 fs and 53 fs, respectively. For comparison, the temporal profile of the uncompressed idler (yellow) from a similar measurement is also overlapped and corresponds to a pulsewidth (FWHM) of 450 fs. (b) The retrieved spectrum (blue) along with the spectral phase (red) of the compressed idler, overlapped with the measured spectrum (gray shaded area), which is limited by the phase-matching bandwidth for SHG in GaSe. Self-normalized (c) measured and (d) retrieved SHG-FROG traces of the compressed idler on a linear scale [90].

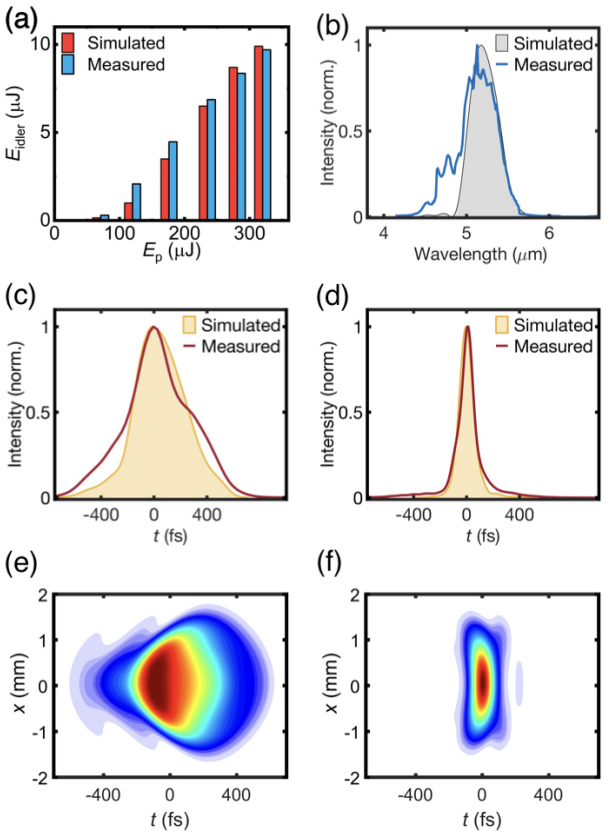


Figure 4.18: Example of comparison between Chi2D simulations and experimental measurements for the idler from the second-stage OPA [90]. The energy-scaling comparison for the uncompressed idler as a function of pump energy ($E_p$) is represented in (a), with practically no energy loss during bulk compression with anti-reflection-coated Ge window. Corresponding to the SHG-FROG measurement shown in Fig. 4.17, (b) denotes the spectral profile comparison, whereas (c) and (d) denote the uncompressed and compressed temporal profile comparison, respectively. The spatio-temporal simulation output corresponding to (c) and (d) are shown in (e) and (f), respectively.

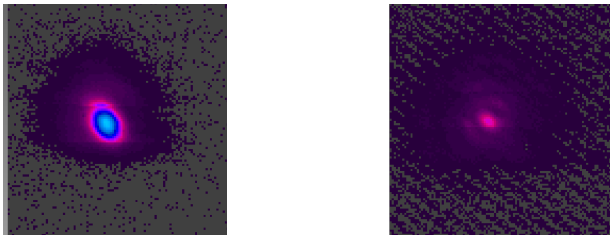


Figure 4.19: Beam profiles of the idler after the 2nd OPA stage before (a) and after (b) insertion of the 30-mm thick Ge window. The beam size of the idler before (a) and after compression (b) validates the simulation in figure 4.18 (e) and (f).

# 5

# CONCLUSION AND OUTLOOK

## 5.1 CONCLUSION

In conclusion, this thesis demonstrates the development of a compact parallel cascaded ZGP-based OPA system.

The first main part of this work is to realize SC generation in a bulk medium, driven with 3-ps 2-$\mu$m laser pulses. We apply very loose-focusing geometry to resolve the damage issue to prevent avalanche ionization when pumped with long-duration MIR pulses. Since the critical power to initiate SC generation in bulk (via self-focusing) is proportional to the square of the driving wavelength ($\propto \lambda^2$ ), the critical pump energy required to obtain critical power with a 3-ps 2-$\mu$m laser pulse is at least ten times higher than that of conventional femtosecond laser pulses at 0.8 or 1$\mu$m. It leads to a drastically detrimental increase of pump fluence under common focal conditions. By applying an extremely loose-focusing geometry (NA < 0.005) to decelerate the rapid growth of plasma density, SC generation was achieved without damaging the crystal. Comparisons of SC generation in different crystals, i.e. YAG, ZnSe, and GaAs, are conducted.

Thanks to the success of SC generation in bulk media on pumping with multi-picosecond MIR pulses, the 3-ps 2-$\mu$m regenerative amplifier can be used as a promising candidate for driving the ZGP-based DFG/OPA stages. The high-power Ho:YLF regenerative amplifier is advantageous to the development of the aimed OPA system. Firstly, the complexity of the system, such as intermediate OPA stages or extra DFG stages employed after the front-end oscillator, is simplified. Secondly, poor wavelength tunability resulting from a limited capability of seed generation over a broad spectral range is mitigated. Thirdly, the pumping energy for DFG/OPAs is scalable to facilitate the higher energy output of the tunable MIR system.

In terms of the preparation for the construction of the DFG/OPA stages, we firstly simulated the OPA process in the ZGP crystal by comparing different combinations of crystal length, pump/seed intensity as well as spatial and temporal overlapping ratio. The major concern here in the simulations is to avoid back conversion, which will induce a large amount of high order dispersion (such as TOD) to impair the compressibility of the output from the DFG/OPA stages. A comfortable parameter zone is mapped out through systematic simulations over a wide range.

In order to fulfill the experimental requirements, a pair of cascaded twin OPA lines are constructed. The SC seed is split and fed into the two OPA lines as the signal for the OPA processes. Both the lines are able to generate a tunable central wavelength of the idler independently within the range of 5 - 8 $\mu$m (corresponding signal: 3500 nm - 2760 nm ). The combined energy of the signal and the idler is 60 $\mu$J. Further energy amplification is feasible. A representative compressed 105-fs pulse at 5.2 $\mu$m is realized by simply inserting a highly transparent bulk Ge to compensate for the residual negative GDD in the idler.

## 5.2 Outlook

The work summarized above testifies the feasibility of 2 $\mu$m-pumped $ZnGeP_2$-based optical parametric amplifiers and it paves the way for further potential applications in various research fields.

### 5.2.1 *Further improvements*

Further improvements in terms of the energy of the outputs, the spectral cover range, and the stability of its performance can be conducted.

The energy of the idler or the signal, on the one hand, can be further improved by upgrading the 2-$\mu$m regenerative amplifier with additional cascaded booster stages, so that the increase of the energy of multi-picosecond 2-$\mu$m output up to a few tens of millijoules may be achieved. On the other hand, with sufficient energy from the high-energy 2-$\mu$m pump, additional cascaded

OPA stages with large-aperture ZGP crystals can be constructed so that the overall gain of the parametric amplification can be further increased. Moreover, to increase the pulse energy of the outputs, the parametric amplification can be switched from the OPA to an OPCPA configuration. By chirping the pulses to adjust the temporal overlap ratio between the signal and the pump, we can optimize the performance of the system in terms of the pulse energy.

The spectral cover range of the idler can be extended into long-wave infrared (LWIR) (> 8 $\mu$m) by replacing with different non-linear crystals, such as LGS, GaSe, which perform better in the parametric amplification in the LWIR range.

The stability of the entire laser system is limited by the pump laser at 1940 nm for the Ho:YLF regenerative amplifier, which may be upgraded to one with better performance in terms of the stability. Moreover, improvement of the precise and stable control of the temperature of the laser crystals and particularly the humidity of the air inside the laser enclosure is also desirable. Furthermore, pushing and keeping the energy of the pump in the parametric amplification process to the level where the gain is saturated can also diminish the influence of the fluctuation of the SC output on the final OPA outputs.

### 5.2.2 *Future applications*

The performance of our laser system in terms of the pulse energy of the outputs ($\sim 60\mu$J, kHz), along with the provision of easy tenability in the fingerprint regime, surpasses that of most commercial lasers (nJ to $\sim \mu$J). This provides a platform for mode-selective vibrational excitation or concurrent excitation of multiple key vibrational modes for multidimensional spectroscopy, extending to non-linear regimes, given the high-energy output, despite considering losses due to pulse-shaping etc.

Millijoule-level few-cycle MIR pulses have become attractive optical drivers for MIR strong-field physics, such as HHG, LIED, and laser-plasma acceleration. With the help of intense ultrashort MIR pulses, high-harmonic cut-off energies of the order of kilo electron volts with sufficient flux are expected. This has been of

great interest in the emerging field of table-top attosecond time-resolved soft x-ray absorption spectroscopy. Such sources can also be used to resolve structural dynamics of matter via LIED.

# Part II

# APPENDIX

# A

# APPENDIX

## A.1 2 $\mu$m HO-DOPED FIBER SOLITON OSCILLATOR

A schematic of the Ho-doped fiber ring oscillator is shown in Figure A.1. The formation of solitons is realized through the compensation between the negative dispersion from material and the positive dispersion induced by the SPM process. The mode locking is triggered and stabilized with the nonlinear polarization evolution (NPE) technique, which works similarly to a saturable absorber by filtering the rotated polarization induced by the Kerr effect.

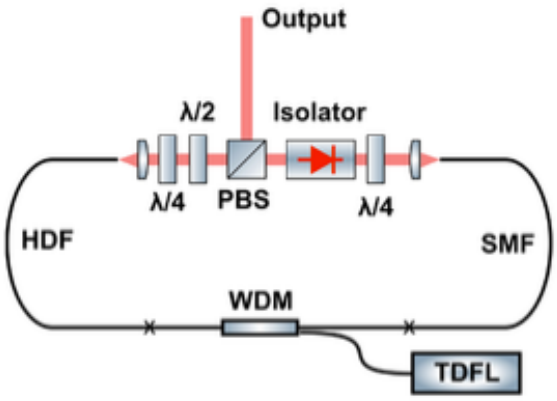


Figure A.1: Schematic of the Ho-doped mode-locking fiber oscillator [92]. HDF: holmium-doped fiber; WDM: wavelength-division multiplexer; SMF: single-mode fiber; TDFL: thulium-doped fiber laser operating at 1950 nm; $\lambda/2$: half-wave plate; $\lambda/4$: quarter-wave plate; PBS: polarizing beam splitter.

The performance of the soliton fiber oscillator is demonstrated in Table A.1

| PARAMETER | PERFORMANCE |
|---|---|
| Central wavelength (nm) | 2040 - 2070 |
| Pulse duration (fs) | 920 |
| Repetition rate (MHz) | 50 |
| Pulse energy (nJ) | 0.8 |
| Bandwidth (nm) | 5-10 |

Table A.1: Parameters of the Ho:fiber soliton oscillator [92].

## A.2 2 $\mu$m HO:YLF REGENERATIVE AMPLIFIER

As depicted in Figure A.2, the Ho:YLF regenerative amplifier is seeded with the stretched output of the 2-$\mu$m Ho:fiber soliton oscillator. Pulse stretching before the amplification and post compression after coupling-out of the cavity are both achieved with two chirped volume Bragg grating (CVBG)s. The amplification of the stretched seeding pulses is determined by the number of the round trips the pulses travel in the cavity, which is controlled by the switch of birefringence in the crystal of the Pockels' cell. Meanwhile, combined with the Faraday isolator and other polarization controlling elements, such as wave-plates and thin film polarisers, the amplified pulses can be coupled out as the polarization becomes orthogonal to that of the input pulses. Our home-built regenerative amplifier is capable of generating 2-$\mu$m pulses with uncompressed pulse energies of 7 mJ at 1 kHz. The pulse duration of the amplified pulses is compressed from 560 ps down to 3 ps with the help of the CVBGs.

## A.3 SHG-FREQUENCY RESOLVED OPTICAL GATING (SHG-FROG)

FROG is a technique to characterize optical pulses in the time-frequency domain by sampling the optical pulses sequentially with a narrower optical gating. The optical gatings are basically from the various nonlinear processes, such as SHG, THG, and so on [93].

The gating function in the SHG-FROG arises from the SHG process. The corresponding gating function is $g(t-\tau) = E(t-\tau)$,

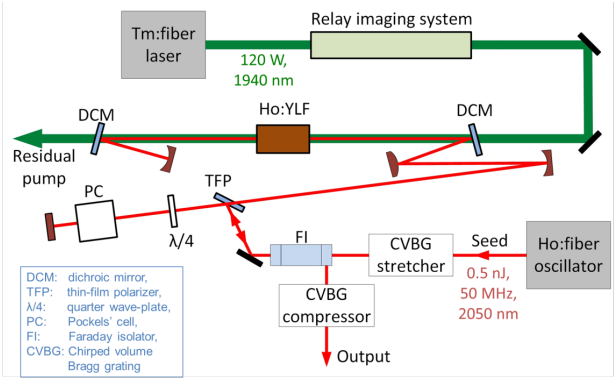


Figure A.2: Schematic of the Ho:YLF regenerative amplifier[37].

where $\tau$ is the scanning delay. The sampled electric field can be described as $E(t)E(t-\tau)$. Thus, the measured FROG trace in the time-frequency domain can be mathematically expressed as follows,

$$I_{FROG}(\omega,\tau) = \left|\int_{-\infty}^{+\infty} E(t)E(t-\tau)exp(-i\omega t)dt\right|^2 \tag{A.1}$$

After the spectrogram trace is measured, the trace is retrieved through the generic algorithm, which compares the assumed electric field with the measured one in the frequency domain until the difference between the measured trace and the retrieved trace is stabilised below a reasonable value, typically 0.5 %. The algorithm is concluded as shown in Figure. A.3.

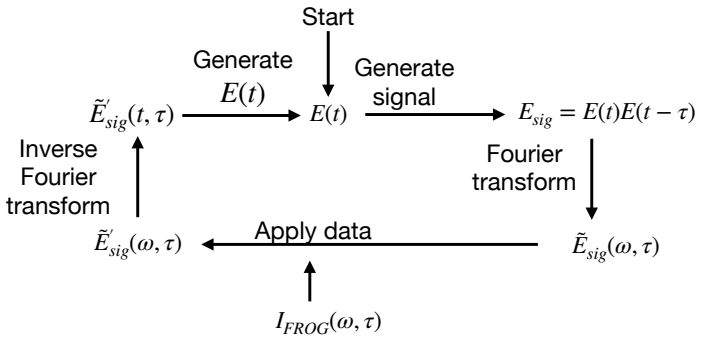


Figure A.3: Schematic of FROG retrieval algorithm from [93].

The setup scheme of SHG-FROG is presented in Figure.A.4. The selection of the SHG crystal depends on the central wavelength of

the laser pulses, BBO (Eksma Optics, 5×5×1 mm, $\theta = 20^o$, $\phi = 90^o$ ), AGS (Eksma Optics, 5×5×1 mm, $\theta = 39^o$, $\phi = 45^o$) or GaSe (Eksma Optics, 7×7×2 mm, z-cut) is inserted for laser pulses at 2 $\mu$m, 3-4 $\mu$m or >4 $\mu$m, respectively. With regard to the laser pulses in MWIR, due to the lack of a compact spectrometer in the MIR region, the MIR spectrograph with a liquid-nitrogen-cooled HgCdTe (MCT) array detector is integrated into the SHG-FROG setup. Representative SHG-FROG results are demonstrated in Figure. 2.7, 4.10 and Figure 4.17.

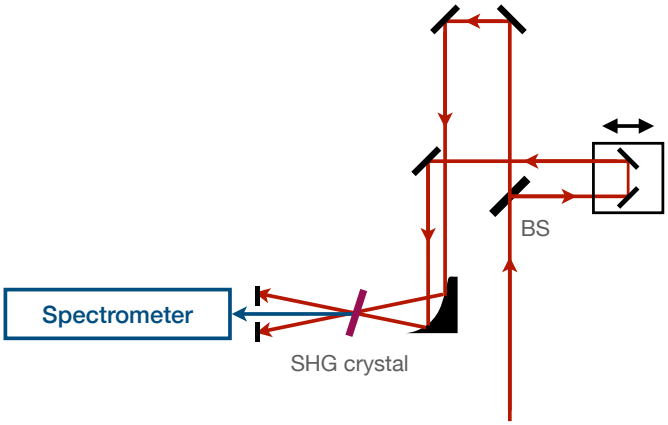


Figure A.4: Schematic of SHG-FROG setup. BS: beam splitter.

# BIBLIOGRAPHY


[1] Tenio Popmintchev, Ming-Chang Chen, Dimitar Popmintchev, Paul Arpin, Susannah Brown, Skirmantas Ališauskas, Giedrius Andriukaitis, Tadas Balčiunas, Oliver D Mücke, Audrius Pugzlys, et al. "Bright coherent ultrahigh harmonics in the keV x-ray regime from mid-infrared femtosecond lasers." In: *science* 336.6086 (2012), pp. 1287–1291.

[2] Cosmin I Blaga, Junliang Xu, Anthony D DiChiara, Emily Sistrunk, Kaikai Zhang, Pierre Agostini, Terry A Miller, Louis F DiMauro, and CD Lin. "Imaging ultrafast molecular dynamics with laser-induced electron diffraction." In: *Nature* 483.7388 (2012), pp. 194–197.

[3] D Woodbury, L Feder, V Shumakova, C Gollner, R Schwartz, B Miao, F Salehi, A Korolov, A Pugžlys, A Baltuška, et al. "Laser wakefield acceleration with mid-IR laser pulses." In: *Optics letters* 43.5 (2018), pp. 1131–1134.

[4] Michael D Fayer. *Ultrafast infrared vibrational spectroscopy*. CRC Press, 2013.

[5] Peter Hamm and Martin Zanni. *Concepts and methods of 2D infrared spectroscopy*. Cambridge University Press, 2011.

[6] Milan Delor, Paul A Scattergood, Igor V Sazanovich, Anthony W Parker, Gregory M Greetham, Anthony JHM Meijer, Michael Towrie, and Julia A Weinstein. "Toward control of electron transfer in donor-acceptor molecules by bond-specific infrared excitation." In: *Science* 346.6216 (2014), pp. 1492–1495.

[7] Cathie Ventalon, James M Fraser, Marten H Vos, Antigoni Alexandrou, Jean-Louis Martin, and Manuel Joffre. "Coherent vibrational climbing in carboxyhemoglobin." In: *Proceedings of the National Academy of Sciences* 101.36 (2004), pp. 13216–13220.

[8] David B Strasfeld, Sang-Hee Shim, and Martin T Zanni. "New advances in mid-IR pulse shaping and its application to 2D IR spectroscopy and ground-state coherent control." In: *Advances in Chemical Physics* 141 (2009), p. 1.

[9] H Pires, M Baudisch, D Sanchez, M Hemmer, and Jens Biegert. "Ultrashort pulse generation in the mid-IR." In: *Progress in Quantum Electronics* 43 (2015), pp. 1–30.

[10] Dong Dong Gu, Wilhelm Meiners, Konrad Wissenbach, and Reinhart Poprawe. "Laser additive manufacturing of metallic components: materials, processes and mechanisms." In: *International materials reviews* 57.3 (2012), pp. 133–164.

[11] Takashi Fujii and Tetsuo Fukuchi. *Laser remote sensing*. CRC press, 2005.

[12] Sergei Tochitsky, Eric Welch, Mikhail Polyanskiy, Igor Pogorelsky, Paris Panagiotopoulos, Miroslav Kolesik, Ewan M Wright, Stephan W Koch, Jerome V Moloney, Jeremy Pigeon, et al. "Megafilament in air formed by self-guided terawatt long-wavelength infrared laser." In: *Nature Photonics* 13.1 (2019), pp. 41–46.

[13] Masamori Endo and Robert F Walter. *Gas lasers*. CRC Press, 2018.

[14] Yi Wu, Fangjie Zhou, Esben W Larsen, Fengjiang Zhuang, Yanchun Yin, and Zenghu Chang. "Generation of 3 mJ, 44 fs, 2.5 micrometer pulses from a single-stage Cr2+: ZnSe amplifier." In: *arXiv preprint arXiv:1910.06650* (2019).

[15] Vyacheslav E Leshchenko, Bradford K Talbert, Yu Hang Lai, Sha Li, Yaguo Tang, Stephen J Hageman, Greg Smith, Pierre Agostini, Louis F DiMauro, and Cosmin I Blaga. "High-power few-cycle Cr: ZnSe mid-infrared source for attosecond soft x-ray physics." In: *Optica* 7.8 (2020), pp. 981–988.

[16] Kyung-Han Hong, Chien-Jen Lai, Jonathas P Siqueira, Peter Krogen, Jeffrey Moses, Chun-Lin Chang, Gregory J Stein, Luis E Zapata, and Franz X Kärtner. "Multi-mJ, kHz, 2.1 $\mu$m optical parametric chirped-pulse amplifier and high-flux soft x-ray high-harmonic generation." In: *Optics letters* 39.11 (2014), pp. 3145–3148.

[17] Nicolas Bigler, Justinas Pupeikis, Stefan Hrisafov, L Gallmann, Christopher R Phillips, and Ursula Keller. "High-power OPCPA generating 1.7 cycle pulses at 2.5 $\mu$m." In: *Optics Express* 26.20 (2018), pp. 26750–26757.

[18] Yanchun Yin, Jie Li, Xiaoming Ren, Yang Wang, Andrew Chew, and Zenghu Chang. "High-energy two-cycle pulses at 3.2 $\mu$m by a broadband-pumped dual-chirped optical parametric amplification." In: *Optics express* 24.22 (2016), pp. 24989–24998.

[19] Yuxi Fu, Kotaro Nishimura, Bing Xue, Akira Suda, Katsumi Midorikawa, and Eiji J Takahashi. "Generation of high-energy mid-infrared pulses via dual-chirped OPA." In: *High-Power, High-Energy, and High-Intensity Laser Technology IV*. Vol. 11033. International Society for Optics and Photonics. 2019, 110330K.

[20] Pengfei Wang, Yanyan Li, Wenkai Li, Hongpeng Su, Beijie Shao, Shuai Li, Cheng Wang, Ding Wang, Ruirui Zhao, Yujie Peng, et al. "2.6 mJ/100 Hz CEP-stable near-single-cycle 4 $\mu$m laser based on OPCPA and hollow-core fiber compression." In: *Optics Letters* 43.9 (2018), pp. 2197–2200.

[21] Giedrius Andriukaitis, Tadas Balčiūnas, Skirmantas Ališauskas, Audrius Pugžlys, Andrius Baltuška, Tenio Popmintchev, Ming-Chang Chen, Margaret M Murnane, and Henry C Kapteyn. "90 GW peak power few-cycle mid-infrared pulses from an optical parametric amplifier." In: *Optics letters* 36.15 (2011), pp. 2755–2757.

[22] Szabolcs Tóth, Roland Flender, Bálint Kiss, Máté Kurucz, Alexey Andrianov, Roland S Nagymihaly, Ludovit Haizer, Eric Cormier, and Károly Osvay. "Comparative study of an ultrafast, CEP-stable, dual-channel mid-IR OPCPA system." In: *JOSA B* 36.12 (2019), pp. 3538–3546.

[23] Nicolas Thiré, Raman Maksimenka, Bálint Kiss, Clément Ferchaud, Pierre Bizouard, Eric Cormier, Károly Osvay, and Nicolas Forget. "4-W, 100-kHz, few-cycle mid-infrared source with sub-100-mrad carrier-envelope phase noise." In: *Optics express* 25.2 (2017), pp. 1505–1514.

[24] C Heese, CR Phillips, BW Mayer, L Gallmann, MM Fejer, and Ursula Keller. "75 MW few-cycle mid-infrared pulses from a collinear apodized APPLN-based OPCPA." In: *Optics express* 20.24 (2012), pp. 26888–26894.

[25] Tsuneto Kanai, Pavel Malevich, Sarayoo Sasidharan Kangaparambil, Kakuta Ishida, Makoto Mizui, Kaoru Yamanouchi, Heinar Hoogland, Ronald Holzwarth, Audrius Pugzlys, and Andrius Baltuska. "Parametric amplification of 100 fs mid-infrared pulses in ZnGeP 2 driven by a Ho: YAG

chirped-pulse amplifier." In: *Optics letters* 42.4 (2017), pp. 683–686.

[26] Lorenz von Grafenstein, Martin Bock, Kevin Zawilski, Peter Schunemann, Uwe Griebner, and Thomas Elsaesser. "Multi-mJ sub-100 fs Midwave-infrared OPCPA at a 1 kHz Repetition Rate." In: *Advanced Solid State Lasers*. Optical Society of America. 2018, AW4A–6.

[27] Pavel Malevich, Tsuneto Kanai, Heinar Hoogland, Ronald Holzwarth, Andrius Baltuška, and Audrius Pugžlys. "Broadband mid-infrared pulses from potassium titanyl arsenate/zinc germanium phosphate optical parametric amplifier pumped by Tm, Ho-fiber-seeded Ho: YAG chirped-pulse amplifier." In: *Optics Letters* 41.5 (2016), pp. 930–933.

[28] D Sanchez, M Hemmer, M Baudisch, SL Cousin, K Zawilski, P Schunemann, O Chalus, C Simon-Boisson, and J Biegert. "7 $\mu$m, ultrafast, sub-millijoule-level mid-infrared optical parametric chirped pulse amplifier pumped at 2 $\mu$m." In: *Optica* 3.2 (2016), pp. 147–150.

[29] Ugaitz Elu, Tobias Steinle, Daniel Sanchez, Luke Maidment, Kevin Zawilski, Peter Schunemann, Uwe D Zeitner, Christophe Simon-Boisson, and Jens Biegert. "Tabletop high-energy 7 um OPCPA and 260 mJ Ho: YLF pump laser." In: *arXiv preprint arXiv:1906.08163* (2019).

[30] Derrek J Wilson, Adam M Summers, Stefan Zigo, Brandin Davis, Seyyed-Javad Robatjazi, Jeffery A Powell, Daniel Rolles, Artem Rudenko, and Carlos A Trallero-Herrero. "An intense, few-cycle source in the long-wave infrared." In: *Scientific reports* 9.1 (2019), pp. 1–7.

[31] Houkun Liang, Peter Krogen, Zhou Wang, Hyunwook Park, Tobias Kroh, Kevin Zawilski, Peter Schunemann, Jeffrey Moses, Louis F DiMauro, Franz X Kärtner, et al. "High-energy mid-infrared sub-cycle pulse synthesis from a parametric amplifier." In: *Nature communications* 8.1 (2017), pp. 1–9.

[32] Peter Krogen, Houkun Liang, K Zawilski, P Schunemann, T Lang, U Morgner, Jeffrey Moses, Franz X Kärtner, and Kyung-Han Hong. "Octave-spanning 1.5-optical-cycle 6.5-$\mu$m OPA pumped by 2.1-$\mu$m OPCPA." In: *CLEO: Science and Innovations*. Optical Society of America. 2016, STu3I–4.

[33] Giedre Marija Archipovaite, Guangyu Fan, Pavel Malevich, Tan Lihao, Stéphane Petit, Jean-Christophe Delagnes, Eric Cormier, Giedrius Andriukaitis, Edgar Kaksis, Andrius Baltuška, et al. "High Energy, Few-Cycle Parametric Source Tunable in the 5–11 $\mu$m Window Driven by an Yb Bulk CPA System." In: *CLEO: Science and Innovations*. Optical Society of America. 2018, SF1N–3.

[34] Bo-Han Chen, Emanuel Wittmann, Yuya Morimoto, Peter Baum, and Eberhard Riedle. "Octave-spanning single-cycle middle-infrared generation through optical parametric amplification in LiGaS2." In: *Opt. Express* 27.15 (2019), pp. 21306–21318.

[35] Shizhen Qu, Houkun Liang, Kun Liu, Xiao Zou, Wenkai Li, Qi Jie Wang, and Ying Zhang. "9 $\mu$m few-cycle optical parametric chirped-pulse amplifier based on LiGaS2." In: *Opt. Lett.* 44.10 (2019), pp. 2422–2425.

[36] U. Elu, T. Steinle, D. Sánchez, L. Maidment, K. Zawilski, P. Schunemann, U. D. Zeitner, C. Simon-Boisson, and J. Biegert. "Table-top high-energy 7 $\mu$m OPCPA and 260 mJ Ho:YLF pump laser." In: *Opt. Lett.* 44.13 (2019), pp. 3194–3197.

[37] Peter Kroetz, Axel Ruehl, Gourab Chatterjee, Anne-Laure Calendron, Krishna Murari, Huseyin Cankaya, Peng Li, Franz X Kärtner, Ingmar Hartl, and RJ Dwayne Miller. "Overcoming bifurcation instability in high-repetition-rate Ho: YLF regenerative amplifiers." In: *Optics letters* 40.23 (2015), pp. 5427–5430.

[38] Lorenz von Grafenstein, Martin Bock, Dennis Ueberschaer, Kevin Zawilski, Peter Schunemann, Uwe Griebner, and Thomas Elsaesser. "5 $\mu$m few-cycle pulses with multi-gigawatt peak power at a 1 kHz repetition rate." In: *Optics Letters* 42.19 (2017), pp. 3796–3799.

[39] Martin Bock, Lorenz von Grafenstein, Uwe Griebner, and Thomas Elsaesser. "Generation of millijoule few-cycle pulses at 5 $\mu$m by indirect spectral shaping of the idler in an optical parametric chirped pulse amplifier." In: *JOSA B* 35.12 (2018), pp. C18–C24.

[40] Giedre Marija Archipovaite, Pavel Malevich, Eric Cormier, Tan Lihao, Andrius Baltuška, and Tadas Balčiūnas. "Efficient few-cycle mid-IR pulse generation in the 5-11 $\mu$m

window driven by an Yb amplifier." In: *Advanced Solid State Lasers*. Optical Society of America. 2017, AM4A–4.

[41] Lorenz von Grafenstein, Martin Bock, Dennis Ueberschaer, Kevin Zawilski, Peter Schunemann, Uwe Griebner, and Thomas Elsaesser. "5 $\mu$m few-cycle pulses with multi-gigawatt peak power at a 1 kHz repetition rate." In: *Optics Letters* 42.19 (2017), pp. 3796–3799.

[42] L Von Grafenstein, M Bock, D Ueberschaer, U Griebner, and T Elsaesser. "Ho: YLF chirped pulse amplification at kilohertz repetition rates–4.3 ps pulses at 2 $\mu$m with GW peak power." In: *Optics letters* 41.20 (2016), pp. 4668–4671.

[43] RR Alfano and SL Shapiro. "Emission in the region 4000 to 7000 Å via four-photon coupling in glass." In: *Physical Review Letters* 24.11 (1970), p. 584.

[44] Andrius Baltuška, Takao Fuji, and Takayoshi Kobayashi. "Controlling the carrier-envelope phase of ultrashort light pulses with optical parametric amplifiers." In: *Physical review letters* 88.13 (2002), p. 133901.

[45] Nathalie Picqué and Theodor W Hänsch. "Frequency comb spectroscopy." In: *Nature Photonics* 13.3 (2019), pp. 146–157.

[46] Ferenc Krausz and Misha Ivanov. "Attosecond physics." In: *Reviews of Modern Physics* 81.1 (2009), p. 163.

[47] Krishna Murari, GJ Stein, H Cankaya, Benoît Debord, Frédéric Gérôme, G Cirmi, OD Mücke, P Li, A Ruehl, I Hartl, et al. "Kagome-fiber-based pulse compression of mid-infrared picosecond pulses from a Ho: YLF amplifier." In: *Optica* 3.8 (2016), pp. 816–822.

[48] LV Keldysh et al. "Ionization in the field of a strong electromagnetic wave." In: *Sov. Phys. JETP* 20.5 (1965), pp. 1307–1314.

[49] A Couairon, E Brambilla, T Corti, D Majus, O de J Ramírez-Góngora, and Miroslav Kolesik. "Practitioner's guide to laser pulse propagation models and simulation." In: *The European Physical Journal Special Topics* 199.1 (2011), pp. 5–76.

[50] Arnaud Couairon and André Mysyrowicz. "Femtosecond filamentation in transparent media." In: *Physics reports* 441.2-4 (2007), pp. 47–189.

[51] BB Zhou, Xing Liu, HR Guo, XL Zeng, XF Chen, HP Chung, Yen-Hung Chen, and Morten Bache. "Parametrically tunable soliton-induced resonant radiation by three-wave mixing." In: *Physical review letters* 118.14 (2017), p. 143901.

[52] Binbin Zhou and Morten Bache. "Invited Article: Multiple-octave spanning high-energy mid-IR supercontinuum generation in bulk quadratic nonlinear crystals." In: *Apl Photonics* 1.5 (2016), p. 050802.

[53] Audrius Dubietis and Arnaud Couairon. *Ultrafast supercontinuum generation in transparent solid-state media*. Springer, 2019.

[54] Audrius Dubietis, Gintaras Tamošauskas, Rosvaldas Šuminas, Vytautas Jukna, and Arnaud Couairon. "Ultrafast supercontinuum generation in bulk condensed media (Invited Review)." In: *arXiv preprint arXiv:1706.04356* (2017).

[55] J Galinis, G Tamošauskas, I Gražulevičiūtė, E Keblytė, V Jukna, and A Dubietis. "Filamentation and supercontinuum generation in solid-state dielectric media with picosecond laser pulses." In: *Physical Review A* 92.3 (2015), p. 033857.

[56] Ieva Gražulevičiūtė, Milda Skeivytė, Enrika Keblytė, Justinas Galinis, Gintaras Tamošauskas, and Audrius Dubietis. "Supercontinuum generation in YAG and sapphire with picosecond laser pulses." In: *Lithuanian Journal of Physics* 55.2 (2015).

[57] PB Corkum, PP Ho, RR Alfano, and JT Manassah. "Generation of infrared supercontinuum covering 3–14 $\mu$m in dielectrics and semiconductors." In: *Optics letters* 10.12 (1985), pp. 624–626.

[58] Rotem Kupfer, Hernan J Quevedo, Herbie L Smith, Luc A Lisi, Ganesh Tiwari, Christopher G Richmond, BB Bowers, L Fang, and BM Hegelich. "Cascade random-quasi-phase-matched harmonic generation in polycrystalline ZnSe." In: *Journal of Applied Physics* 124.24 (2018), p. 243102.

[59] JJ Pigeon, S Ya Tochitsky, C Gong, and C Joshi. "Supercontinuum generation from 2 to 20 $\mu$m in GaAs pumped by picosecond CO 2 laser pulses." In: *Optics letters* 39.11 (2014), pp. 3246–3249.

[60] Laurent Gallais and Mireille Commandré. "Laser-induced damage thresholds of bulk and coating optical materials at 1030 nm, 500 fs." In: *Applied optics* 53.4 (2014), A186–A196.

[61] F Silva, DR Austin, A Thai, M Baudisch, M Hemmer, D Faccio, A Couairon, and J Biegert. "Multi-octave supercontinuum generation from mid-infrared filamentation in a bulk crystal." In: *Nature communications* 3.1 (2012), pp. 1–5.

[62] A. Couairon, L. Sudrie, M. Franco, B. Prade, and A. Mysyrowicz. "Filamentation and damage in fused silica induced by tightly focused femtosecond laser pulses." In: *Phys. Rev. B* 71 (12 2005), p. 125435.

[63] A. Couairon and A. Mysyrowicz. "Femtosecond filamentation in transparent media." In: *Physics Reports* 441.2 (2007), pp. 47–189. ISSN: 0370-1573.

[64] Yong-Nian Xu and W. Y. Ching. "Electronic structure of yttrium aluminum garnet ($Y_3Al_5O_{12}$)." In: *Phys. Rev. B* 59 (16 1999), pp. 10530–10535.

[65] F. Silva, D. R. Austin, A. Thai, M. Baudisch, M. Hemmer, D. Faccio, A. Couairon, and J. Biegert. "Multi-octave supercontinuum generation from mid-infrared filamentation in a bulk crystal." In: *Nature Communications* 3 (2012), p. 807.

[66] Jonathan B. Ashcom, Rafael R. Gattass, Chris B. Schaffer, and Eric Mazur. "Numerical aperture dependence of damage and supercontinuum generation from femtosecond laser pulses in bulk fused silica." In: *J. Opt. Soc. Am. B* 23.11 (2006), pp. 2317–2322.

[67] Siqi Cheng, Gourab Chatterjee, Friedjof Tellkamp, Axel Ruehl, and RJ Dwayne Miller. "Multi-octave supercontinuum generation in YAG pumped by mid-infrared, multi-picosecond pulses." In: *Optics letters* 43.18 (2018), pp. 4329–4332.

[68] Lukáš Indra et al. "Picosecond pulse generated supercontinuum as a stable seed for OPCPA." In: *Opt. Lett.* 42.4 (2017), pp. 843–846.

[69] Alexandr Špaček, Lukáš Indra, František Batysta, Petr Hříbek, Jonathan T Green, Jakub Novák, Roman Antipenkov, Pavel Bakule, and Bedřich Rus. "Stability mechanism of picosecond supercontinuum in YAG." In: *Optics Express* 28.14 (2020), pp. 20205–20214.

[70] Julius Darginavičius, Donatas Majus, Vytautas Jukna, Nail Garejev, Gintaras Valiulis, Arnaud Couairon, and Audrius Dubietis. "Ultrabroadband supercontinuum and third-harmonic generation in bulk solids with two optical-cycle carrier-envelope phase-stable pulses at 2 $\mu$m." In: *Optics Express* 21.21 (2013), pp. 25210–25220.

[71] J. J. Pigeon, S. Ya. Tochitsky, C. Gong, and C. Joshi. "Supercontinuum generation from 2 to 20 $\mu$m in GaAs pumped by picosecond $CO_2$ laser pulses." In: *Opt. Lett.* 39.11 (2014), pp. 3246–3249.

[72] Govind P Agrawal. "Nonlinear fiber optics." In: *Nonlinear Science at the Dawn of the 21st Century*. Springer, 2000, pp. 195–211.

[73] KV Lvov, S Yu Stremoukhov, EA Migal, and FV Potemkin. "Asymmetric temporal splitting of laser pulse and broad supercontinuum generation under femtosecond filamentation in YAG crystal." In: *Laser Physics Letters* 15.8 (2018), p. 085402.

[74] AA Lanin, AA Voronin, EA Stepanov, AB Fedotov, and AM Zheltikov. "Multioctave, 3–18 $\mu$m sub-two-cycle supercontinua from self-compressing, self-focusing soliton transients in a solid." In: *Optics Letters* 40.6 (2015), pp. 974–977.

[75] Qing Wang, Jinwei Zhang, Alexander Kessel, Nathalie Nagl, Vladimir Pervak, Oleg Pronin, and Ka Fai Mak. "Broadband mid-infrared coverage (2–17 $\mu$m) with few-cycle pulses via cascaded parametric processes." In: *Optics letters* 44.10 (2019), pp. 2566–2569.

[76] Jinwei Zhang, Kilian Fritsch, Qing Wang, Ferenc Krausz, Ka Fai Mak, and Oleg Pronin. "Intra-pulse difference-frequency generation of mid-infrared (2.7–20 $\mu$m) by random quasi-phase-matching." In: *Optics letters* 44.12 (2019), pp. 2986–2989.

[77] Andreas Vaupel, Nathan Bodnar, Benjamin Webb, Lawrence Shah, and Martin C Richardson. "Concepts, performance review, and prospects of table-top, few-cycle optical parametric chirped-pulse amplification." In: *Optical Engineering* 53.5 (2013), p. 051507.

[78] Lorenz von Grafenstein. "Generation of Intense Few-Cycle Pulses in the Mid-Wave Infrared." PhD thesis. Humboldt-Universität zu Berlin, 2018.

[79] Ondřej Novák, Peter R Krogen, Tobias Kroh, Tomáš Mocek, Franz X Kärtner, and Kyung-Han Hong. "Femtosecond 8.5 $\mu$m source based on intrapulse difference-frequency generation of 2.1 $\mu$m pulses." In: *Optics letters* 43.6 (2018), pp. 1335–1338.

[80] Marvin J Weber. *Handbook of optical materials*. Vol. 19. CRC press, 2002.

[81] S Chaitanya Kumar, PG Schunemann, KT Zawilski, and M Ebrahim-Zadeh. "Advances in ultrafast optical parametric sources for the mid-infrared based on CdSiP 2." In: *JOSA B* 33.11 (2016), pp. D44–D56.

[82] O Chalus, PG Schunemann, KT Zawilski, J Biegert, and M Ebrahim-Zadeh. "Optical parametric generation in CdSiP 2." In: *Optics letters* 35.24 (2010), pp. 4142–4144.

[83] Christian Gaida, Martin Gebhardt, Tobias Heuermann, Fabian Stutzki, Cesar Jauregui, Jose Antonio-Lopez, Axel Schülzgen, Rodrigo Amezcua-Correa, Andreas Tünnermann, Ioachim Pupeza, et al. "Watt-scale super-octave mid-infrared intrapulse difference frequency generation." In: *Light: Science & Applications* 7.1 (2018), pp. 1–8.

[84] Arlee V Smith. "SNLO nonlinear optics code." In: *Sandia National Laboratories, Albuquerque, NM* 87185.1423 (2004), p. 87.

[85] Robert A Kaindl, Matthias Wurm, Klaus Reimann, Peter Hamm, Andrew M Weiner, and Michael Woerner. "Generation, shaping, and characterization of intense femtosecond pulses tunable from 3 to 20 $\mu$m." In: *JOSA B* 17.12 (2000), pp. 2086–2094.

[86] Giulio Cerullo and Sandro De Silvestri. "Ultrafast optical parametric amplifiers." In: *Review of scientific instruments* 74.1 (2003), pp. 1–18.

[87] Suk Kyoung Lee, Arthur G Suits, H Bernhard Schlegel, and Wen Li. "A reaction accelerator: Mid-infrared strong field dissociation yields mode-selective chemistry." In: *The journal of physical chemistry letters* 3.18 (2012), pp. 2541–2547.

[88] David B Strasfeld, Sang-Hee Shim, and Martin T Zanni. "Controlling vibrational excitation with shaped mid-IR pulses." In: *Physical review letters* 99.3 (2007), p. 038102.

[89] T Lang, A Harth, J Matyschok, T Binhammer, M Schultze, and U Morgner. "Impact of temporal, spatial and cascaded effects on the pulse formation in ultra-broadband parametric amplifiers." In: *Optics Express* 21.1 (2013), pp. 949–959.

[90] Siqi Cheng, Gourab Chatterjee, Friedjof Tellkamp, Tino Lang, Axel Ruehl, Ingmar Hartl, and RJ Dwayne Miller. "Compact Ho: YLF-pumped ZnGeP 2-based optical parametric amplifiers tunable in the molecular fingerprint regime." In: *Optics Letters* 45.8 (2020), pp. 2255–2258.

[91] Stefan Witte and Kjeld SE Eikema. "Ultrafast optical parametric chirped-pulse amplification." In: *IEEE Journal of Selected Topics in Quantum Electronics* 18.1 (2011), pp. 296–307.

[92] Peng Li, Axel Ruehl, Colleen Bransley, and Ingmar Hartl. "Low noise, tunable Ho: fiber soliton oscillator for Ho: YLF amplifier seeding." In: *Laser Physics Letters* 13.6 (2016), p. 065104.

[93] Rick Trebino. *Frequency-resolved optical gating: the measurement of ultrashort laser pulses*. Springer Science & Business Media, 2012.

# DECLARATION

Hiermit versichere ich an Eides statt, die vorliegende Dissertationsschrift selbst verfasst und keine anderen als die angegebenen Hilfsmittel und Quellen benutzt zu haben.

Die eingereichte schriftliche Fassung entspricht der auf dem elektronischen Speichermedium.

Die Dissertation wurde in der vorgelegten oder einer ähnlichen Form nicht schon einmal in einem früheren Promotionsverfahren angenommen oder als ungenügend beurteilt.

*Hamburg, 15.12.2020*

Siqi Cheng